



HAL
open science

New X-Ray Microtomography Setups and Optimal Scan Conditions to Investigate Methane Hydrate-Bearing Sand Microstructure

Thi Xiu Le, Patrick Aïmediou, Michel Bornert, Baptiste Chabot, Andrew King, Anh Minh A.M. Tang

► To cite this version:

Thi Xiu Le, Patrick Aïmediou, Michel Bornert, Baptiste Chabot, Andrew King, et al.. New X-Ray Microtomography Setups and Optimal Scan Conditions to Investigate Methane Hydrate-Bearing Sand Microstructure. *Geotechnical Testing Journal*, 2021, 10.1520/GTJ20190355 . hal-03053626

HAL Id: hal-03053626

<https://enpc.hal.science/hal-03053626>

Submitted on 11 Dec 2020

HAL is a multi-disciplinary open access archive for the deposit and dissemination of scientific research documents, whether they are published or not. The documents may come from teaching and research institutions in France or abroad, or from public or private research centers.

L'archive ouverte pluridisciplinaire **HAL**, est destinée au dépôt et à la diffusion de documents scientifiques de niveau recherche, publiés ou non, émanant des établissements d'enseignement et de recherche français ou étrangers, des laboratoires publics ou privés.

1 **New X-ray microtomography setups and optimal scan conditions to investigate**
2 **methane hydrate-bearing sand microstructure**

3 *Thi Xiu Le, Patrick Aïmediou, Michel Bornert, Baptiste Chabot, Andrew King, Anh*
4 *Minh Tang**

5 *Laboratoire Navier, Ecole des Ponts ParisTech, CNRS UMR 8205, Univ. Gustave*
6 *Eiffel, Marne-la-Vallée, France*

7 **Corresponding authors:*

8

9 *Dr. Anh Minh Tang*

10 *6-8 avenue Blaise Pascal, 77455 Champs-sur-Marne, France*

11 anh-minh.tang@enpc.fr

12 *Dr. Thi Xiu Le*

13 *6-8 avenue Blaise Pascal, 77455 Champs-sur-Marne, France*

14 thi-xiu.le@enpc.fr

15 *Dr. Patrick Aïmediou*

16 *6-8 avenue Blaise Pascal, 77455 Champs-sur-Marne, France*

17 patrick.aimedieu@enpc.fr

18 *Dr. Michel Bornert*

19 *6-8 avenue Blaise Pascal, 77455 Champs-sur-Marne, France*

20 michel.bornert@enpc.fr

21 *Baptiste Chabot*

22 *6-8 avenue Blaise Pascal, 77455 Champs-sur-Marne, France*

23 Baptiste.Chabot@enpc.fr

24 *Dr. Andrew King*

25 *Synchrotron Soleil, D306, Route de Belle Image, l'Orme des Merisiers, 91190 Saint-*
26 *Aubin, France*

27 king@synchrotron-soleil.fr

28

29 **Abstract**

30 Methane hydrates, naturally formed at high pressure and low temperature in marine
31 and permafrost sediments, represent a great potential energy resource but also a
32 considerable geo-hazard and climate change source. Investigating the grain-scale
33 morphology of methane hydrate-bearing sandy sediments is crucial for the
34 interpretation of geophysical data and reservoir-scale simulations in the scope of
35 methane gas production as methane hydrate morphologies and distribution within the
36 porous space significantly impact their macroscopic physical/mechanical properties.
37 X-ray computed tomography (XRCT) and Synchrotron X-Ray computed tomography
38 (SXRCT) are commonly used to analyze the microstructure of geo-materials.
39 However, methane hydrates exist only at high pressure (up to several MPa) and low
40 temperature (a few °C). This article describes the development of three experimental
41 setups, which aim at creating methane hydrates in sandy sediment, adapted to XRCT
42 and SXRCT observations. The advantages and drawbacks of each setup are
43 discussed. The discussions focus on the effects of the choice of the system to control
44 temperature and pressure on the quality of images. The obtained results would be
45 useful for future works involving temperature and/or pressure control systems
46 adapted to XRCT and SXRCT observations of various geo-materials.

47 *Keywords:* Methane hydrate-bearing sand, X-ray computed tomography (XRCT),
48 synchrotron XRCT, experimental setups, scans conditions, high pressure, low
49 temperature.

50 **Introduction**

51 Methane hydrates (MHs), being solid ice-like compounds of methane gas and water,
52 are naturally formed at high pressure and low temperature in marine and permafrost
53 settings. They are being considered as an alternative energy resource but also a
54 source of geo-hazards and climate change (Collett et al. 2009). Depending on the
55 characteristic particle size and the effective stress, different morphologies and pore
56 distribution within natural sediments of methane hydrates, such as nodules/chunks,
57 lenses/veins or pore-filling have been identified (Boswell et al. 2011; Dai et al. 2012).
58 In the scope of methane gas production from methane hydrate-bearing sediments,
59 currently, due to technical feasibilities, only pore-filling MHs at high hydrate saturation
60 in sandy sediments are being considered. Most experimental works concern
61 laboratory tests on synthetic samples because of challenges to get cored-intact
62 methane hydrate-bearing sediment samples. In the objective of creating synthetic
63 pore-filling methane hydrates in sandy sediments (to mimic natural sediments),
64 different methods have been proposed such as the excess-gas, ice-seeding, or
65 excess-water methods (Clayton et al. 2005; Priest et al. 2009; Waite et al. 2004).
66 However, by using seismic wave velocities (Chand et al. 2004; Dvorkin et al. 2000;
67 Dvorkin and Lavoie 1999; Dvorkin and Nur 1996; Helgerud et al. 1999), MHs are
68 believed to exist in four idealized arrangements or “pore-habits”: cement, with grain-
69 grain contacts; cement, with mineral coating; load-bearing and pore-filling. Physical
70 and mechanical properties of sediments containing MHs depend considerably on
71 methane hydrate morphologies and distribution within the pore space, which are thus
72 of the essence for interpretation of geophysical data and reservoir-scale simulations
73 in the scope of methane gas production (Taleb et al. 2018; Le et al. 2019; Nguyen-Sy

74 et al. 2019; Alavoine et al. 2020; Taleb et al. 2020). Therefore, pore-scale
75 observations of MH morphologies and pore-habits in sandy sediments are crucial.

76

77 Laboratory X-ray computed tomography (XRCT) and Synchrotron X-Ray Computed
78 Tomography (SXRCT) have been extensively used to investigate the 3D
79 microstructure of gas hydrate-bearing sediments (Chaouachi et al. 2014, Kerkar et al.
80 2009; Kerkar et al. 2014; Ta et al. 2015; Zhao et al. 2015). Studying synthetic
81 methane hydrate-bearing sand (MHBS) with these techniques is really challenging
82 due to not only the need of special experimental setups (i.e. high pressure and low
83 temperature should be maintained) but also to the poor image contrast between
84 methane hydrate and water, which depends mainly on the difference of material
85 density and atomic number. To improve XRCT/SXRCT image contrast, other
86 gas/fluid (Tetrahydrofuran-THF, Carbon dioxide-CO₂ or Xenon-Xe) and/or saline
87 water solutions (Sodium chloride-NaCl, Barium chloride-BaCl₂, Potassium iodide-KI)
88 have been used (Chaouachi et al. 2014, Kerkar et al. 2009; Kerkar et al. 2014; Ta et
89 al. 2015; Chen and Espinoza, 2018). By using gas/fluid different from methane,
90 experimental setups are less complicated. For instance, there is no need of pressure
91 control for the THF hydrate (THF hydrate can be formed at atmospheric pressure)
92 while lower pressure and/or higher temperature are needed for studies of CO₂ or Xe
93 hydrates. Note that gas hydrate morphology depends on the type of gas/fluid used.
94 Furthermore, the phase boundary of methane hydrate formation is shifted depending
95 on salt concentration contained in water Sloan and Koh (2008) and salt exclusion
96 during gas hydrate formation increases the salt concentration in the remaining water.

97

98 Concerning XRCT image, spatial resolution mainly depends on the distances
99 between the source, the object and the detector. Complex experimental setups of
100 MHBS studies usually limit the image spatial resolution to avoid the collision between
101 the source, the experimental setup and the detector. Morphologies and pore habits of
102 methane hydrate formed in sandy sediments following the excess-gas method (MHs
103 are formed by injecting methane gas into an unsaturated sandy sediment) have been
104 investigated previously by Yang et al. (2015) and Zhao et al. (2015). Within voxel size
105 of 25 μm , it was impossible to directly observe MHs as the voxel size was in the
106 same order of magnitude as the size of the largest MH crystals. By using a
107 conventional segmentation method based on gray levels (which are, as a first
108 approximation, proportional to material density), methane hydrates were found to be
109 formed at gas-water interfaces, floating between sand grains without coating grain
110 surfaces (a water layer was found to envelop grain surfaces). However, image noise
111 and partial volume effect (gray levels of voxels at interfaces of different phases are
112 intermediate between the gray levels of the different phases) did influence the
113 segmentation and the attributed phases (morphologies and pore habits of methane
114 hydrates).

115

116 Note that reported XRCT scans were usually performed at the end of the gas hydrate
117 formation process in sandy sediments as the scanning time is long (several hours).
118 Within the high temporal resolution of SXRCT (a few minutes), the formation and
119 growth of gas hydrate in sandy sediments could be captured over time.

120

121 In the present study, three experimental setups have been developed in the objective
122 of investigating pore-scale morphologies and pore habits of MHs in sandy sediments
123 via XRCT and SXRCT. Their designs aim at improving the image contrast and the
124 image spatial resolution. As CT images can hardly differentiate pure water from
125 methane hydrate, saline water (i.e. KI solution) was used to better distinguish the
126 liquid phase and methane hydrate when both coexist. Furthermore, efforts have been
127 made to enhance the image spatial resolution in order to distinguish methane hydrate
128 from the liquid phase (either tap or saline water) on the basis of their morphology
129 (regular water menisci or more complex geometry of MH). In the following sections,
130 the optimization of XRCT scan conditions for MHBS is first described. Afterwards, the
131 three experimental setups and their corresponding advantages and drawbacks are
132 discussed.

133

134 **Optimization of scan conditions**

135 Absorption XRCT and SXRCT consist in exposing an object to X-rays from multiple
136 orientations (by rotating the sample in this study) and measuring the intensity
137 decrease for all source-detector paths. Gray levels of the obtained radiographic
138 images, after calibration, quantify the attenuation of the sample, *i.e.* reflect the
139 proportion of X-rays absorbed/scattered as they pass through the object. More
140 precisely, X-ray attenuation follows a Beer-Lambert type law (Swinehart 1962), which
141 involves the linear attenuation coefficient (μ). Different phases in the object can be
142 well distinguished if their attenuation coefficients are significantly different from each
143 other. Indeed, μ is a function of the energy of X-rays. In a polychromatic setup (as for

144 XRCT), the gray levels of the image result from a complex average of μ , which is
145 relative to the used energy range.

146

147 Lei et al. (2018) used potassium iodide solutions and in-line propagation-based
148 phase-contrast CT analysis of X-ray attenuation and diffraction for pore-scale
149 visualization of MHBS with XRCT. In the present study, theoretical ratios of μ of
150 different phases (methane gas, pure water, methane hydrate, saline water, quartz)
151 are first calculated in order to quantify the induced contrast between phases on the
152 image gray scale (see Figure 1). For the considered materials, sand grains are the
153 most absorbing objects while methane gas is the least absorbing. We thus plot the
154 absorption of the other phases (water, MHs and saline water) in a normalized scale
155 where 1 corresponds to grains and 0 corresponds to gaz. The XCOM program
156 established by the National Institute of Standards and Technology (NIST XCOM)
157 provides the mass attenuation coefficients (μ/ρ) of various compounds for various
158 values of photon energy. These data allowed plotting the curves corresponding to
159 water/quartz and methane hydrate/quartz shown in Figure 1. For the saline solutions
160 (*i.e.* Potassium iodide KI), the value of the mass attenuation coefficient of the solution
161 is obtained according to a simple addition:

162
$$\mu/\rho = \sum_i w_i (\mu/\rho)_i \quad (1)$$

163 where w_i is the mass proportion of the component i (water or salt) and ρ is the unit
164 mass, being for water and Potassium iodide (KI) equal to 1 and 3.12 (Mg/m³),
165 respectively. The results obtained for the KI solution of 2, 3.5 and 5 wt% are also
166 plotted in Figure 1. Note that the adopted density of quartz, methane gas, methane
167 hydrate and water is 2.65, 0.0007, 0.9 and 1 Mg/m³ respectively.

169 Figure 1 shows that, for the whole considered energy range (10-200 keV, which
170 corresponds to typical energies considered in a laboratory XRCT setup), there is
171 almost no difference between the ratio of pure water/quartz and that of methane
172 hydrate/quartz (red and black curves). The difference in gray level of these two
173 phases is in the order of image noise (which typically varies from 2 % to 10 % of gray
174 level range). That explains the difficulty in distinguishing methane hydrate from water
175 in a XRCT image. For the case of KI solutions (blue curves), their ratios are
176 significantly different from that of methane hydrate in the range of photon energy
177 higher than 33 keV where an absorption edge is observed. At a concentration of 5 %
178 for KI, the maximum ratio is close to 1 (*i.e.* saline solution absorbs almost as quartz)
179 while at 2 % of concentration, the increase in contrast (allowed by the KI solution) is
180 moderate. Therefore, saline water of 3.5 % of KI by weight was chosen in this study
181 so that saline water can be optimally distinguished from both methane hydrate and
182 sand grain. More precisely, for energies between 33 and 60 keV, the gray level of
183 saline solution would be at equal distance from quartz and MH, optimizing the image
184 contrast. Note that the laboratory XRCT source is a polychromatic source with a wide
185 energy spectrum with a maximal energy corresponding to the prescribed electron
186 beam acceleration voltage. However, its maximum intensity, due to the
187 Bremsstrahlung effect, is somewhat below that maximum. Furthermore, to avoid
188 beam hardening artifacts in XRCT images and more specifically to reduce X-rays
189 below 33 keV, a copper filter (Cu) was used to eliminate low energy X-rays. Relative
190 transmission of X-ray intensity $\exp(-\mu_{Cu} \times t_{Cu} - \mu_{Al} \times t_{Al})$ of two cases of copper
191 thickness (t_{Cu}), is also shown in Figure 1 (Aluminum tube thickness, t_{Al} is 2×0.89
192 mm). In the present study, a Cu filter with a thickness of 0.1 mm was used for the

193 scans to preserve a higher X-ray flux in the energy range of 30 – 100 keV where the
194 linear attenuation coefficient ratio of the KI solution at 3.5 wt% is well separated from
195 that of methane hydrate.

196

197 Preliminary scans at abovementioned optimized conditions (acceleration voltage of
198 source was 80 or 100 keV; 0.1 mm thick Cu filter) were done. Typical close views of
199 cross sections of 3D images obtained on mixtures of dry sand with either pure water
200 or saline water compacted in an aluminum tube (exterior diameter, $d_{ext.} = 6.45$ mm;
201 thickness, $t = 0.89$ mm) are shown in Figure 2. For the case of sand wetted with pure
202 water, Figure 2a, the mean gray levels of each phase were determined from the gray
203 level profiles along the yellow line in Figure 2a, plotted in Figure 3a: $G_a = 21100$ (for
204 air, A); $G_q = 22700$ (for quartz, Q); $G_w = 21600$ (for pure water, W). Similarly, for the
205 case of sand wetted with saline water (Figure 2b), Figure 3b shows: $G_a = 12400$; G_q
206 $= 14150$; $G_{sw} = 13400$ (saline water, SW). The ratios of water, $R_{w/q}$ and of saline
207 water, $R_{sw/q}$ were calculated as follows:

$$208 \quad R_{w/q} = (G_w - G_a) / (G_q - G_a) \quad (2)$$

$$209 \quad R_{sw/q} = (G_{sw} - G_a) / (G_q - G_a) \quad (3)$$

210 According to profiles shown in Figure 3, $R_{w/q}$ is equal 0.3 while $R_{sw/q}$ equal 0.6.
211 Furthermore, it is expected that the ratio of methane hydrate/quartz is close to that of
212 water/quartz. These scan conditions should be then appropriate for MHBS scans,
213 with an optimal contrast between air, MH, saline water and quartz (relative gray
214 levels equal 0, 0.3, 0.6, and 1, respectively).

215

216 Unlike conventional laboratory XRCT, the so-called “pink beam” SXRCT makes use
217 of a narrower energy spectrum, which is more concentrated around a mean energy.
218 Details of effective linear attenuation coefficient has been defined in the work of Lei
219 et al. (2018). Preliminary SXRCT scans (typical cross sections shown in **Erreur !**
220 **Source du renvoi introuvable.**) were performed at the Psiche beamline at the
221 French synchrotron SOLEIL (King et al. 2016) run in pink mode with a mean energy
222 of 44 keV. $R_{w/q}$ and $R_{sw/q}$ are 0.25 and 0.6 respectively (Figure 5). These values are
223 close to the theoretical estimations at 44 keV (see Figure 1). Note that the Paganin
224 filter (Paganin et al. 2002), designed to account for and partly correct phase contrast
225 artifacts, has been used during the image reconstruction. It can also be noticed from
226 profiles in Figures 3 and 5 that noise levels are significantly lower in SXRCT images
227 than in XRCT ones.

228

229 **Experimental setup investigations**

230 **Materials and methodology**

231 The sediment used in this study was Fontainebleau silica sand (NE34). Classified as
232 SP according to the Unified Soil Classification System (USCS), it consists of quartz
233 grains having a diameter ranging from 100 to 300 microns. Tap water and saline
234 solution (KI with concentration of 3.5 %) were used for the test. Standard purity of the
235 used methane gas was 99.995 %. The characteristics of tap water provided by the
236 supplier are: total chlorine 0.48 mg(Cl₂)/L; pH 7.7; electrical conductivity (at 25 °C)
237 609 μS/cm; total iron < 10 μg/L; total aluminum 53 μg/L. In the present work, we
238 consider that the salinity and the total dissolved solids in the tap water are negligible.

239

240 Moist sand was first compacted by tamping in layers into an aluminum tube (exterior
241 diameter, $d_{\text{ext}} = 6.45$ mm; thickness, $t = 0.89$ mm). Aluminum was chosen instead of
242 beryllium as used in other studies (e.g. Lei et al. 2018) to facilitate the manipulation
243 because of the toxicity of beryllium. The initial water content was fixed in the range
244 between 10-15 % with an accuracy of $\pm 0.1\%$. In the present work, we consider that
245 the initial water content does not influence the quality of the obtained images. The
246 average porosity (volume of gas and liquid phases divided by total volume of the
247 sample) was estimated at 0.40 by segmenting several 3D images obtained on the
248 samples at various locations (see Le 2019, for more details about the segmentation
249 technique). Both high pressure and low temperature (2-3 °C; 7 MPa) were
250 maintained for the MH formation.

251

252 To maintain low temperature, cooled air was circulated around the aluminum tube.
253 Compressed air was cooled down by using a combination of chilled water (controlled
254 by a cryostat) and a heat exchanger. Cooled air temperature, as well as sample
255 temperature, were controlled via the compressed air flow rate (by imposing a
256 compressed air pressure). Note that air was chosen instead of liquids for the
257 temperature control to avoid additional X-ray absorption. In addition, preliminary
258 experiments with wet sand showed an identical temperature (measured by
259 thermocouples) in the air, outside of the aluminum tube, and that in the wet sand, at
260 the center of the aluminum tube, at the same height.

261

262 Methane gas was injected into the sample to maintain a high methane gas pressure.
263 It is supposed that methane gas pressure is constant in a closed system once the

264 MH formation is finished (no need of additional methane gas for further MH
265 formation). Therefore, at the end of the MH formation when the media are supposed
266 to be stable, there is no need to control methane gas pressure during the XRCT
267 scans. However, when the purpose is to follow the MH formation over time by
268 SXRCT scans, methane gas pressure needs to be controlled and maintained
269 constant during the whole process.

270

271 The above thermal and pressure conditions were maintained during the laboratory
272 XRCT scans, which lasted about 12 hours each to avoid MH dissociation. A generic
273 view of various experimental setups developed in this purpose is shown in Figure 6.
274 The sample was fixed on a turntable for scans. An Ultratom micro-tomography setup,
275 from RX Solutions, using either a Hamamatsu L10801 micro-focus reflection (230
276 keV) or a Hamamatsu L10712 nano-focus (160 keV) transmission X-ray source
277 together with a Paxscan Varian 2520V flat-panel imager (1920x1560 pixels², pixel
278 size of 127 μm), was used for the laboratory XRCT scans. At an optimized Source
279 Detector Distance (SDD), governed by the divergence of the X-Ray cone-beam of the
280 X-Ray source in use, a smaller Source Object Distance (SOD) would provide a
281 higher spatial resolution (or a smaller voxel size).

282

283 Furthermore, SXRCT scans were performed at the Psiche beamline at the French
284 synchrotron SOLEIL (King et al. 2016) with a mean energy of 44 keV. Voxel size was
285 0.9 μm and the scan time 12-15 minutes. Paganin filter was optimized to limit the
286 phase contrast at the interfaces between constitutive phases so that gray level of
287 each phase in the images remains almost homogenous (apart from noise).

288

289 In the present study, three setups have been developed. The details of each of them,
290 their advantages and drawbacks and the obtained results are presented in the
291 following sections.

292

293 **Experimental setup No. 1**

294

295 Figure 7 shows the first setup used for XRCT scans of MHBS. A poly-methyl-
296 methacrylate tube (PMMA tube; exterior diameter, $d_{ext} = 24$ mm; thickness, $t = 3.5$
297 mm) was fixed around the aluminum tube for the cooled-air circulation from its bottom
298 to its top. A manometer was fixed at the top of the aluminum tube to monitor methane
299 gas pressure in the tube. The aluminum tube height was chosen to avoid collision
300 between the manometer and the X-ray source during the scan (the distance from the
301 turntable to the top of the aluminum tube is 430 mm, see Figure 7). Note that both
302 XRCT sources available on the Ultratom setup can be used. A thermocouple was
303 installed between the aluminum tube and the PMMA one at the middle of its height.
304 Methane gas at 7 MPa was injected during the MH formation by a pressure
305 controller, which was connected to a gas flowmeter. These conditions were
306 maintained during two days for the MH formation. At the end of the MH formation,
307 pressure controller and gas flowmeter were removed, and all the valves were closed
308 prior to the transportation of the whole system to the XRCT room.

309

310 A cooling gel was wrapped around the PMMA tube during the cell transportation
311 (which lasted about five minutes during which the cooled-air circulation had to be cut

312 off) to avoid MH dissociation. The cooled-air circulation around the aluminum tube
313 was reset as quickly as possible once the cell was installed inside the XRCT room.
314 Sample pressure and temperature were verified before the scan. The Source Object
315 Distance (SOD) was limited by the exterior diameter of the PMMA tube ($SOD \geq 20$
316 mm to maintain a security distance of 8 mm). Dry compressed-air flow was shifted
317 towards the PMMA tube to avoid water condensation during scans (anti-
318 condensation system). Both aluminum and PMMA tubes were rotated together to
319 maintain sample temperature during the scan. The soft tube bringing cooled air from
320 the heat exchanger to the PMMA tube needed to be flexible and long enough to
321 rotate with the PMMA tube.

322

323 Twelve tests have been performed with this setup, among which however, only a few
324 gave images exhibiting good enough quality to be used to characterize
325 microstructure (about 40 %). Indeed, it turned out that the cell slightly vibrated during
326 the scans because of the turbulent cooled-air flow. These vibrations induced
327 fluctuations of the CT geometry whose amplitude were too large for an accurate CT
328 reconstruction. The obtained 3D images were thus blurred, with very unsharp edges.
329 An example of an unsuccessful scan is shown in Figure 8. Gray levels within the
330 constitutive phases, including grains, were not homogenous. MH morphology
331 observation was then impossible. An example of a successful scan is shown in
332 Figure 9 (voxel size was $5 \mu\text{m}$). The image shows an assembly of sand grains (light
333 gray), the pore space filled with methane gas (black) and methane hydrates (gray).
334 MHs can be observed at grain contacts and also on grain surfaces. The mean gray
335 level of each phase was determined from the gray level profiles (as illustrated in
336 **Erreur ! Source du renvoi introuvable.**10): $G_a = 22500$ (for air, A); $G_q = 33000$ (for

337 quartz, Q) and $G_{mh} = 26500$ (for methane hydrate, MH). The ratio $R_{mh/q}$ is equal to
338 0.38, similar to the expected ratio. Furthermore, the standard deviations of the quartz
339 and methane gas phases are close (700). Signal to noise ratio (SNR) was estimated
340 at $(33000 - 22500)/700 = 1/0.067$.

341

342 **Experimental setup No. 2**

343

344 In order to improve the image spatial resolution, the setup No. 2 (shown in Figure 11)
345 has been designed. First, to further reduce the SOD, the PMMA tube (used in the
346 setup No. 1) was removed. The nano-focus source was used instead of the micro-
347 focus one, and the aluminum tube was placed closer to it during the scans: SOD was
348 8 mm instead of 20 mm in the setup No. 1. A Polyvinyl Chloride (PVC) support was
349 fixed to the source and enveloped the aluminum tube. Temperature control was
350 ensured by a circulation of cooled air inside this PVC support, again from the bottom
351 to the top. A thin Kapton film was used to thermally isolate the source (and in
352 particular its thin window) and to protect it from the cooled air. Within this system,
353 only the aluminum tube was rotated during the scans while the PVC support was
354 fixed. A smaller air flow rate (compressed air pressure was about 200 kPa compared
355 to 360 kPa for the setup No. 1) was needed to maintain a similar sample
356 temperature. Actually the heat flux from ambient air through the soft tube walls,
357 between the heat exchanger and the cooled-air inlet, was lower (in particular
358 because of a shorter soft tube length). In addition, the manometer was fixed at the
359 bottom of the cell and the aluminum tube height was reduced to 320 mm (this
360 minimal length being constrained by the diameter of the nano-focus source). These

361 modifications allowed significantly reducing the amplitude of the vibrations of the
362 aluminum tube during scans.

363

364 Methane hydrates were equally formed in sandy sediments in the laboratory then
365 transported to the XRCT room for scans. The PMMA tube (used for setup No. 1) was
366 placed around the aluminum tube to initially form MHs. Compared to the setup No. 1,
367 the installation of the cell in the XRCT room was more complicated as cooled air can
368 only be circulated when the aluminum tube was enveloped by the PVC support.
369 Sample temperature was maintained by a cooling gel wrapped directly around the
370 aluminum tube during its installation. A thermocouple, fixed on the PVC support (see
371 Figure 11), was used to measure the sample temperature close to the scanned zone.

372

373 As for the first setup, among the ten scans performed with the second setup, only a
374 few provided images with good quality (about 40 %), again because of cell vibrations.
375 An example of successful result is shown in Figure 12 (voxel size was 3.5 μm). MH
376 was more difficultly distinguished from methane gas even with a better image spatial
377 resolution compared to the setup No. 1 (see Figure 9), because in particular of a
378 poorer signal to noise ratio. $R_{mh/q}$ and SNR were estimated at 1/3 and 1/0.085
379 respectively (Figure 13).

380

381 Another possible reason, to explain the heterogeneity of gray levels in the phases, is
382 related to the heterogeneous and porous structure of the PVC support. Indeed, X-
383 rays passed through a thin PVC layer serving for thermal isolation before being
384 captured by the detector. During the calibration stage of the CT scans, which consists

385 in recording various radiographs without sample, the PVC layer crossed by X-rays is
386 not exactly at the same position as during the scans with the sample, which induces
387 additional artifacts. For a further development of setup No. 2, another, more
388 homogeneous material (such as PMMA) should be used between aluminum tube and
389 detector. Actually, PVC was chosen in this study because manufacturing the
390 complex-shaped support with PVC was easier (compared to PMMA).

391

392 **Experimental setup No. 3**

393

394 Within the two first setups, methane hydrates were first formed outside the
395 tomography room and XRCT scans were performed only when the MH formation was
396 stabilized. During the scans, the cell was closed and the temperature was
397 maintained. Setup No. 3 was primarily developed for SXRCT scans which allow one
398 to continuously follow the formation and evolution of MHs. For this reason, methane
399 gas needs to be supplied and its pressure to be monitored during the scans.

400

401 Figure 14 shows the schematic view and a picture of the setup No. 3. A small
402 methane gas bottle (volume of 40 mL) was connected to the methane gas inlet of the
403 cell via a pressure reducer, which reduced the methane gas pressure from 13 MPa
404 inside the bottle to 7 MPa at the gas inlet. This system was used to maintain methane
405 gas pressure in the sample constant at 7 MPa (± 0.1 MPa) during the MH formation
406 and scans.

407

408 Cooled air was circulated between the aluminum and a PMMA tube, similar to the
409 one used in the setup No 1 but somewhat smaller and thinner (exterior diameter, d_{ext}
410 = 23 mm; thickness, $t = 2$ mm), for the temperature control. The cooled-air inlet was,
411 in this setup, at the top of the PMMA tube. The PMMA tube was fixed at its top and
412 thus did not rotate during the scans. The compressed air pressure was in the same
413 order as that used for the setup No. 2. In addition, the aluminum tube height was
414 reduced to 180 mm. Two thermocouples, inserted into the PMMA tube to measure
415 the air temperatures close to the air inlet and outlet, showed a rather stable
416 temperature difference of 1.5 – 2.0 °C during the scans.

417

418 Figure 15 shows a preliminary result obtained by XRCT, with a voxel size of 4 μm .
419 The micro-focus source was used because the geometry of the tube does not allow
420 high resolution. This 15-hour scan was started 28 hours after the start of the
421 experiment, during which temperature and pressure were controlled, when the
422 formation of MH was considered to be stabilized. MH morphologies (crystals/layers)
423 were clearly observed over grain surfaces. Furthermore, $R_{mh/q}$ and SNR were 0.3 and
424 $1/0.095$ respectively (Figure 16). It can be seen that the $R_{mh/q}$ and SNR were in the
425 same order for the three experimental setups. The difference was that successful
426 scan ratios were lower for the two first setups due to cell vibration while this problem
427 was well resolved by using the third one: all five XRCT tests were successful. The
428 setup No. 3 is however not compatible with higher resolution XRCT imaging because
429 of the large diameter of the PMMA tube.

430

431 The setup No. 3 was also successfully used to perform SXRCT scans. An example is
432 shown in Figure 17 (voxel size was 0.9 μm). Really small hydrate particles, formed at

433 the sand grains surface, can be clearly observed. $R_{mh/q}$, $R_{sw/q}$ and SNR were 0.27,
434 0.73 and 1/0.080, respectively (Figure 18). The ratios ($R_{mh/q}$, $R_{sw/q}$) calculated on the
435 image are close to the theoretical ones. A small increase of salt concentration in the
436 remaining saline water during the MH formation caused a slightly higher $R_{sw/q}$ value.

437

438 Furthermore, within the high temporal resolution of SXRCT, the evolution of methane
439 hydrate formation could be followed with time. Figure 19 provides vertical cross-
440 sections through the sample (note that previously shown cross-sections were
441 horizontal) at a same position at various times. Water was initially located at the
442 contacts of sand grains because of the capillary suction (Figure 19a). The air-water
443 interface can be easily identified by the concave meniscus. At 0.8 h from the
444 application of MH formation conditions, these interfaces became irregular and the
445 concave meniscus disappeared. In addition, a thin layer (of water or methane
446 hydrate) appeared on the surface of the grain. As water and methane hydrate have
447 similar gray levels and cannot be distinguished by gray levels, the evolution of their
448 morphology can be used. Actually, irregular interface between the gas phase and
449 water or hydrate phase suggests that this later became a rigid phase (i.e. methane
450 hydrate). Besides, the thin layer appeared on the sand grain surface should
451 correspond to methane hydrate as suggested by Chaouachi et al. (2015). It should
452 be noted that some water was moved out of this area between $t = 0.3 - 0.8$ h. We can
453 then expect that at 0.8 h, methane hydrate was formed at methane gas/water
454 interfaces and at the sand grain surface; MH layers became thicker with time as
455 shown in the Figure 19.

456

457 **Discussions and recommendations**

458 Three experimental setups were developed for pore-scale morphology and pore-habit
459 investigations of MHs in sandy sediments via XRCT and SXRCT. The image spatial
460 resolution was well improved by using SXRCT instead of XRCT. However, SXRCT
461 scans are costly and access time is very limited. Furthermore, by using saline water,
462 methane hydrates could be well distinguished from the remaining water during the
463 MH formation (Figure 17) while for the case of tap water (e.g. Figure 19), methane
464 hydrates and water could only be distinguished from each other via the kinetics of
465 MH formation (MH crystals or layer were grown over time) or via the interface
466 roughness (smooth interface between liquid and gas due to interfacial tension).
467 However, due to the shift of the phase boundary of methane hydrate formation for
468 saline solution, the sample temperature needed to be maintained at a lower
469 temperature compared to that for water (1-2 °C lower at 7 MPa).

470

471 In previous studies where gas hydrate morphology in sediments were investigated,
472 other gas/fluid (THF or Xenon) was used to facilitate the gas hydrate formation
473 because only temperature control (Kerkar et al. 2009) or pressure control (Chen and
474 Espinoza 2018) was required. In the present work, as methane hydrates were
475 investigated, both low temperature and high pressure were required. Furthermore, in
476 order to maintain a low temperature, liquid was usually used in previous studies
477 (Chaouachi et al. 2015; Ta et al. 2015; Zhao et al. 2015; Le et al. 2020). That would
478 avoid the system vibration induced by air flow, as observed in the present work.
479 However, X-ray absorption of water would decrease the image's quality.
480 Furthermore, voxel size in XRCT images, in these studies, was quite large, in a range

481 of 20 μm to 30 μm due to complex and bulky experimental setups, which were
482 required to control both temperature and pressure (Ta et al. 2015; Yang et al. 2015;
483 Zhao et al. 2015). Within such resolution, small particles of MHs could not be
484 observed. Furthermore, the partial volume effect was important. In the present work,
485 a voxel size of 4 μm was obtained by the setup No. 3 with a very good image's
486 quality, even in a laboratory CT setup, MH morphologies (crystals, layers) were thus
487 clearly observed.

488 Besides, Lei et al. (2019) used a Peltier plate for temperature control. Yet, a
489 temperature gradient of 4 $^{\circ}\text{C}$ was measured between the top and bottom of the
490 sample (about 54 mm height), *i.e.* 0.08 $^{\circ}\text{C}/\text{mm}$. By using cooled air in this study, the
491 temperature gradient over 150 mm of the tube height was about 2 $^{\circ}\text{C}$, *i.e.* 0.013
492 $^{\circ}\text{C}/\text{mm}$ which favors the homogeneity of MH formation in the sample. Moreover, by
493 using a small methane gas bottle in this study, associated with a pressure reducer,
494 methane gas pressure was maintained constant during the whole MH formation
495 process.

496

497 Among the three experimental setups developed in the present study, the third one
498 was the most optimized. Actually, the aluminum tube height was shortened to
499 minimize the vibration induced by the air flow. The setup No. 2 has the best spatial
500 resolution for XRCT scans (voxel size equals to 3.5 μm) but its experimental
501 procedure is the most delicate. Besides, the setup No. 2 was compatible only with the
502 Nano-focus source while the two others can be used for all types of X-ray source.

503

504 Concerning the pressure control system, the sample can be disturbed during the
505 system transportation to the XRCT room in the case of the two firsts setups.
506 However, it avoids occupying the room during a long period. The setup No. 3 (using a
507 small methane gas bottle) is the best choice for SXRCT scans. It however requires a
508 setup compatible with large and heavy samples, as the one available on the Psiche
509 beamline.

510

511 **Conclusions**

512 The paper describes the scan condition optimizations and the developments of
513 special experimental setups to investigate pore-scale morphologies and pore-habits
514 of MHBS via XRCT and SXRCT.

515

516 Based on theoretical attenuation coefficient ratios between phases, XRCT scan
517 conditions were optimized (scan energy, filter thickness and saline water solution).
518 Preliminary XRCT and SXRCT scans performed on compacted sand wetted with
519 pure water or saline water confirmed the theoretical estimations.

520

521 Afterward, three experimental setups were developed in the objective of improving
522 the image spatial resolution for pore-scale morphology and pore-habit investigations
523 of MHs in sandy sediments via XRCT and SXRCT. The details of temperature and
524 gas pressure controls were presented. The results obtained for each experimental
525 setup allowed evaluating its performance to observe the morphologies and pore-
526 habits of MHBS. The experimental setup No. 3 seems to be the most appropriate.

527 Sample temperature was controlled by circulating cooled air between the aluminum
528 and the PMMA tube which is fixed at its top. Attention was paid to minimize the cell
529 vibration induced by cooled air flux.

530

531 The choices of temperature and pressure controls presented in the present work can
532 be useful for further studies on MHBS as well as other geo-materials involving a
533 control of temperature and/or gas pressure during XRCT/SXRCT scans.

534

535 **Acknowledgement**

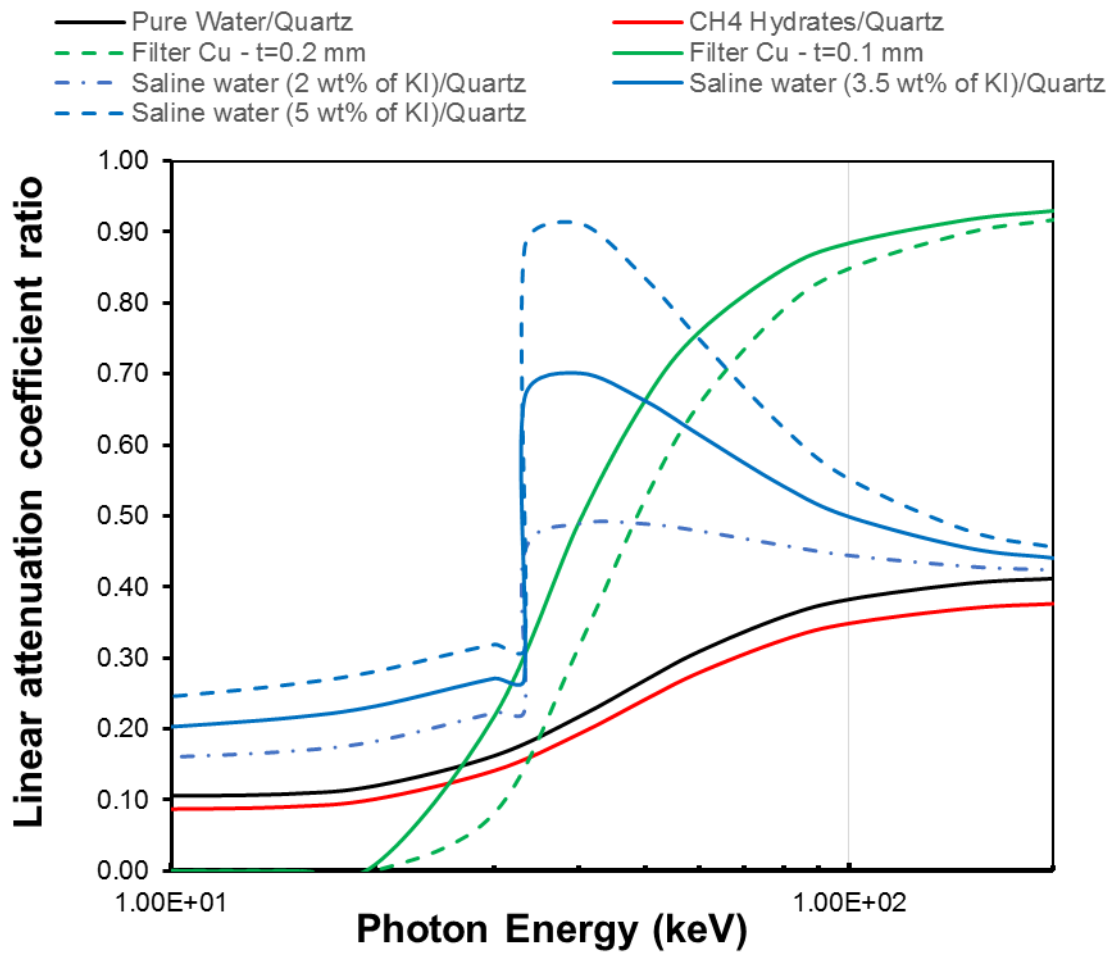
536 The authors would like to express their great appreciation to the French National
537 Research Agency for funding the present study, which is part of the project HYDRE
538 “Mechanical behavior of gas-hydrate-bearing sediments” –ANR-15-CE06-0008.

539 SXRCT images were recorded at the Psiche beamline of Synchrotron Soleil in the
540 context of proposal 20181629.

541 We also would like to express our sincere thanks to Marine Lemaire and Emmanuel
542 Delaure for their technical support.

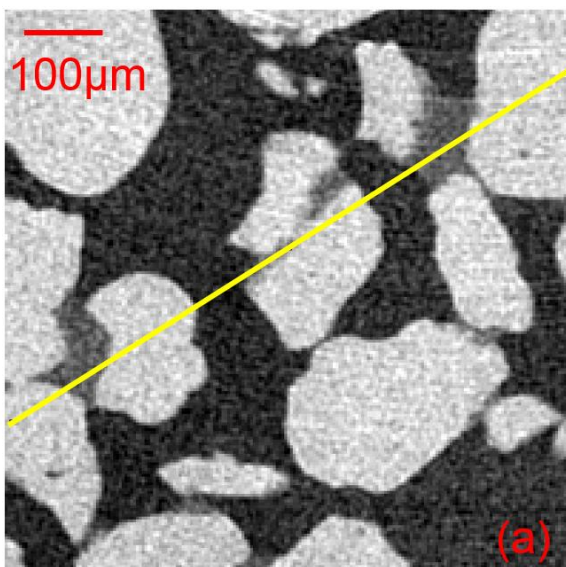
543

544 **Lists of figures**

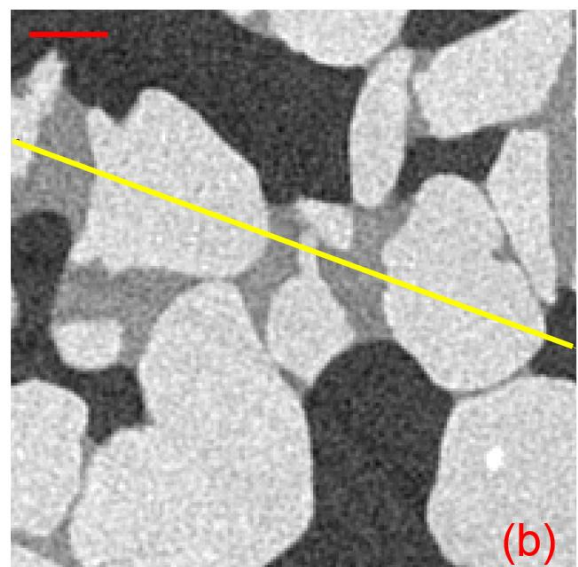


545

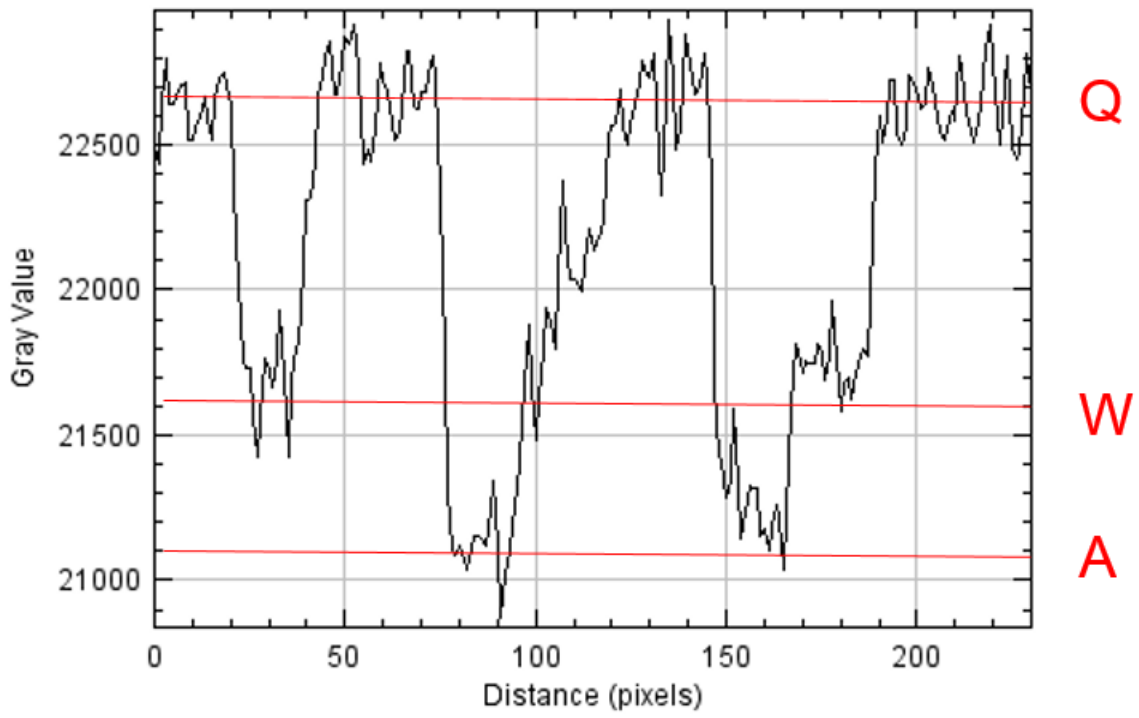
546 Figure 1. Linear attenuation coefficient ratio between phases, and X-Ray
547 transmission through Cu filter, versus photon energy.



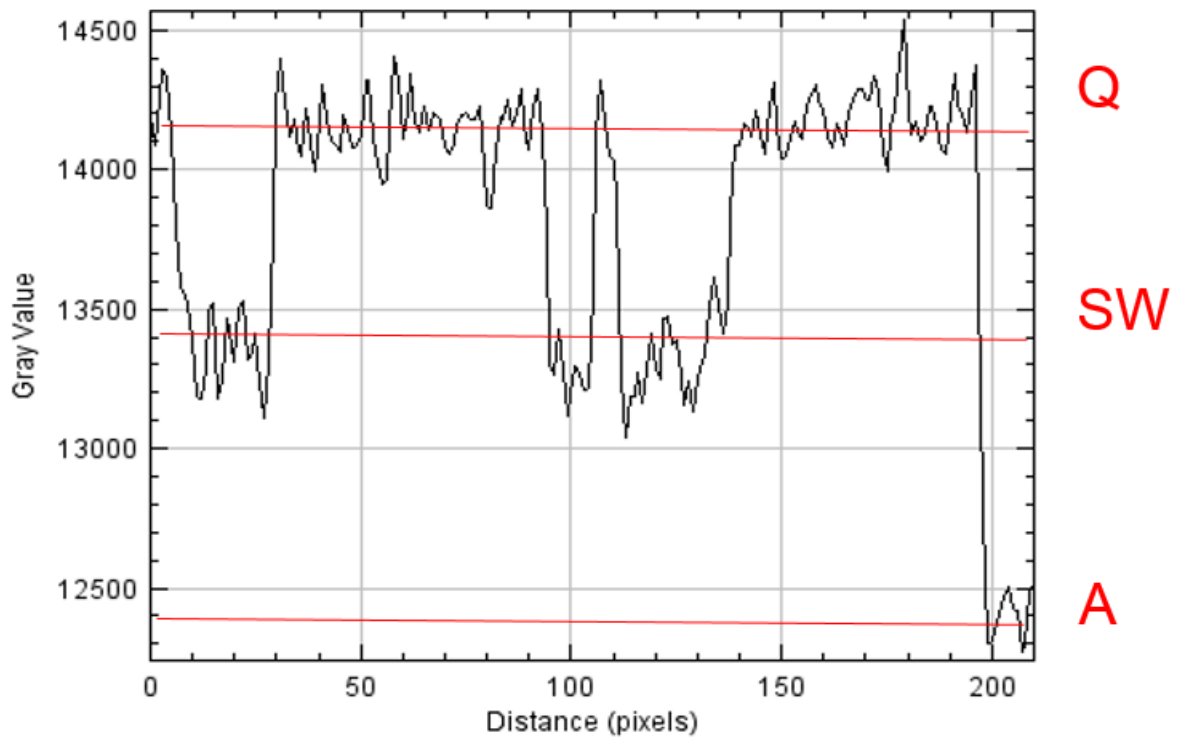
548



549 Figure 2. XRCT images of unsaturated sand with (a) pure water; (b) saline water.

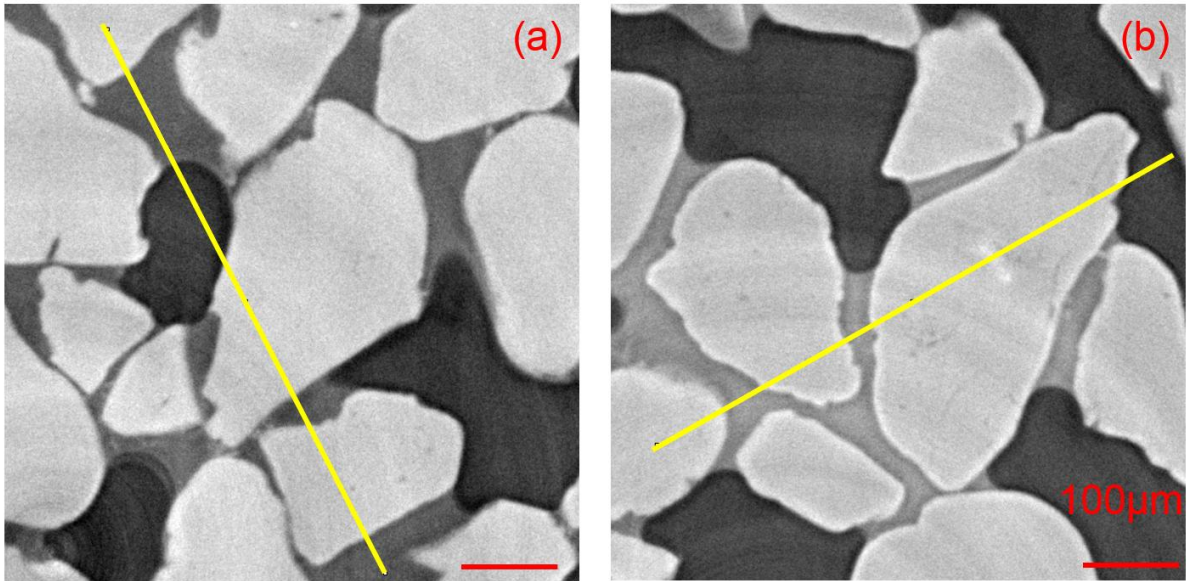


(a)

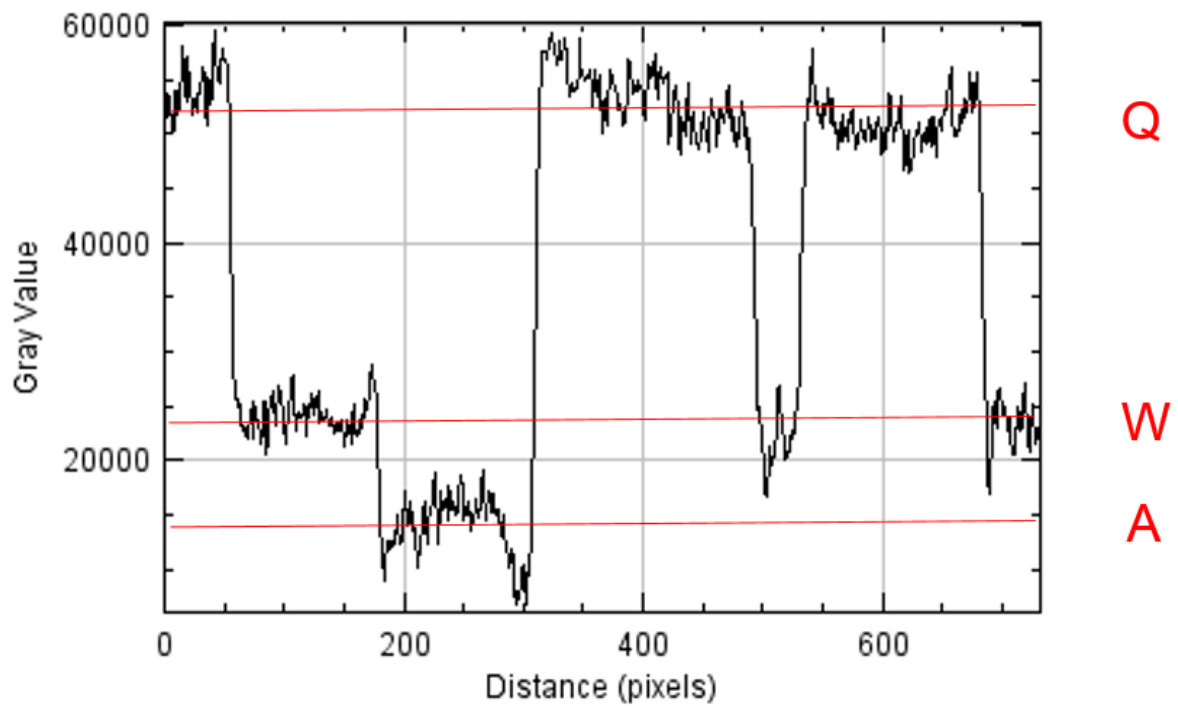


(b)

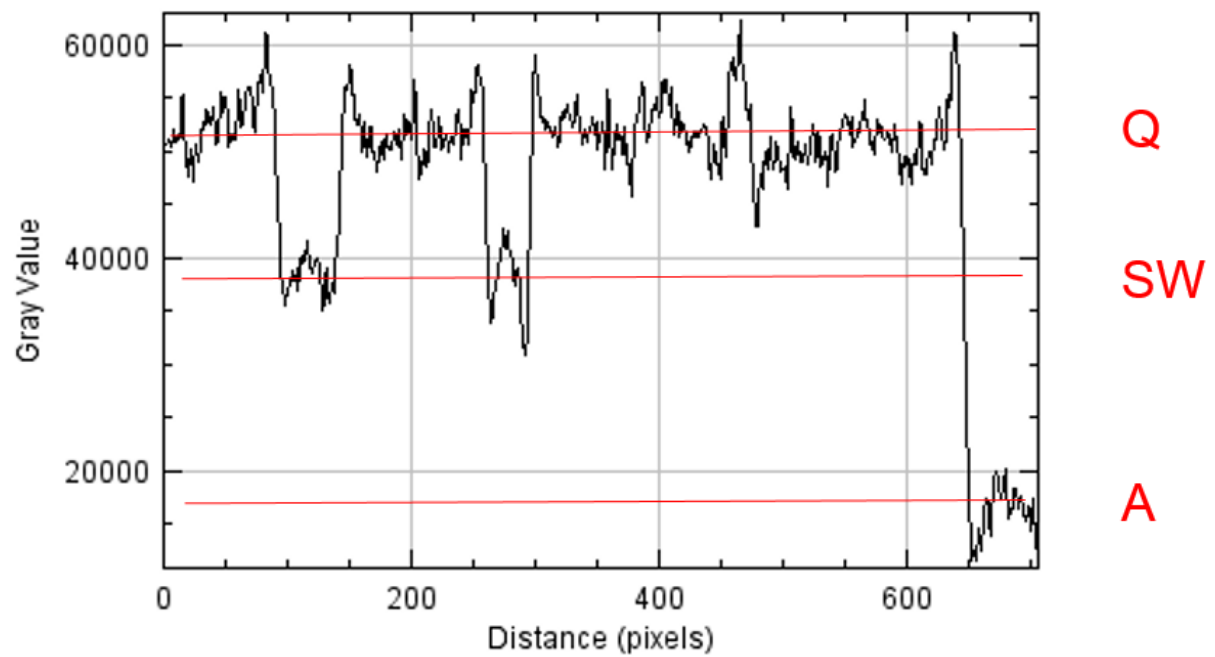
551 Figure 3. Gray level profiles along yellow lines in Figure 2: (a) water/quartz; (b) saline
552 water/quartz.



554 Figure 4. SXRCT images of unsaturated sand with (a) pure water; (b) saline water.



(a)



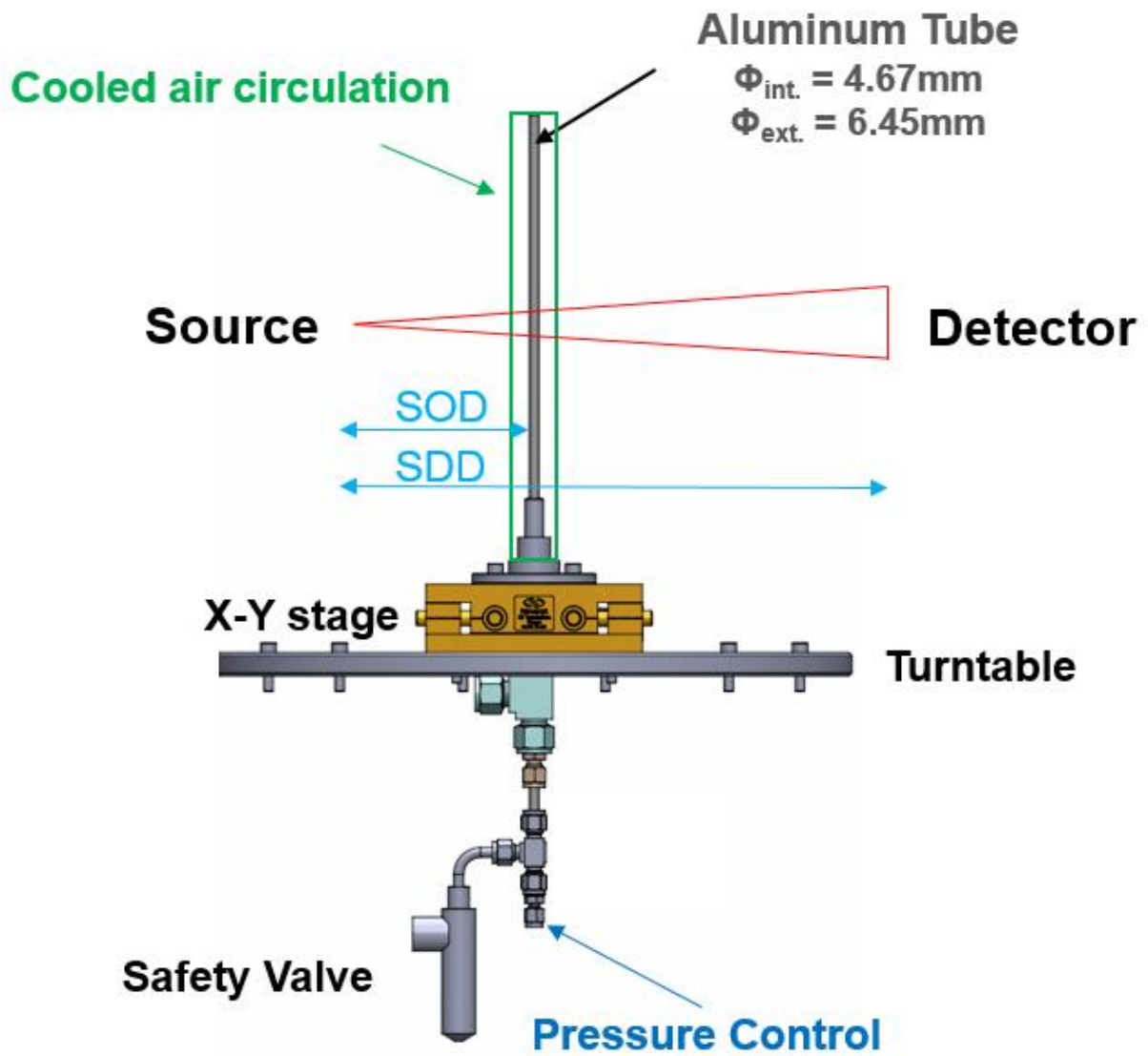
(b)

555

556 Figure 5. Gray level profiles along yellow lines in Figure 4: (a) water/quartz; (b) saline
 557 water/quartz.

558

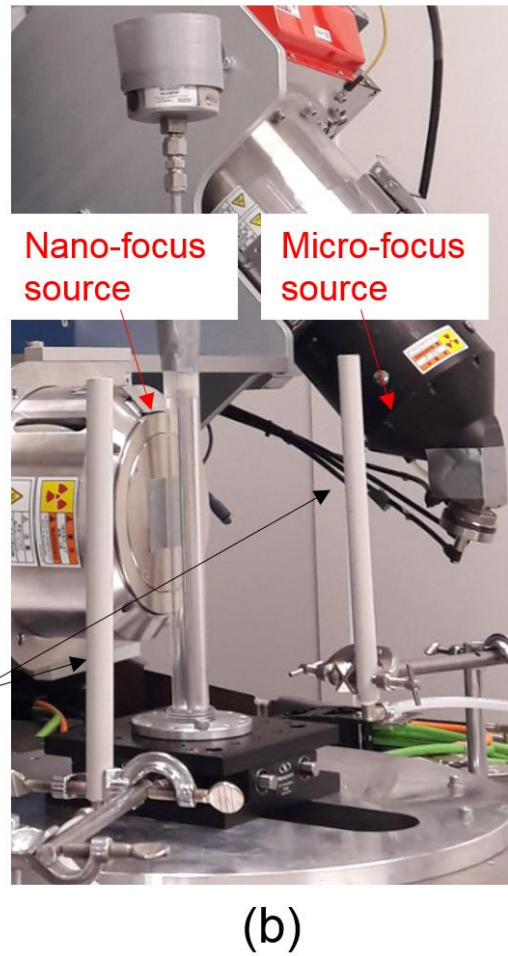
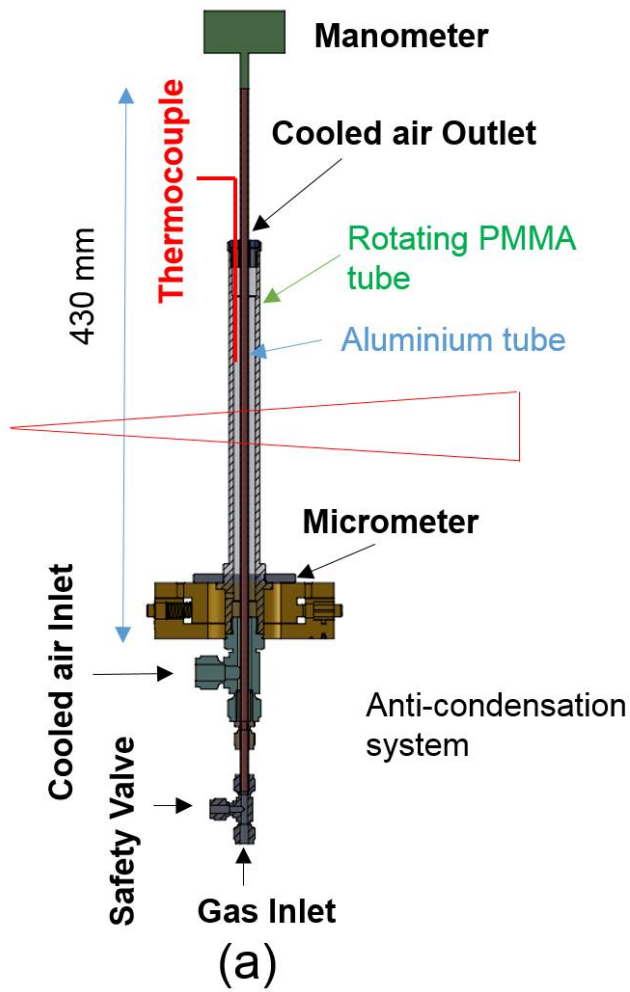
559



561

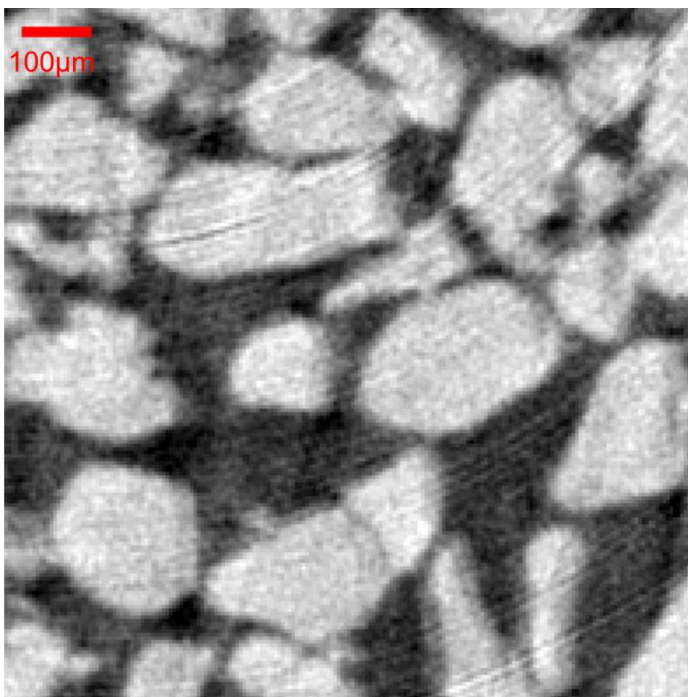
562 Figure 6. Experimental setup principles for XRCT scans of MHBS. SOD: Source

563 Object Distance; SDD: Source Detector Distance.



564

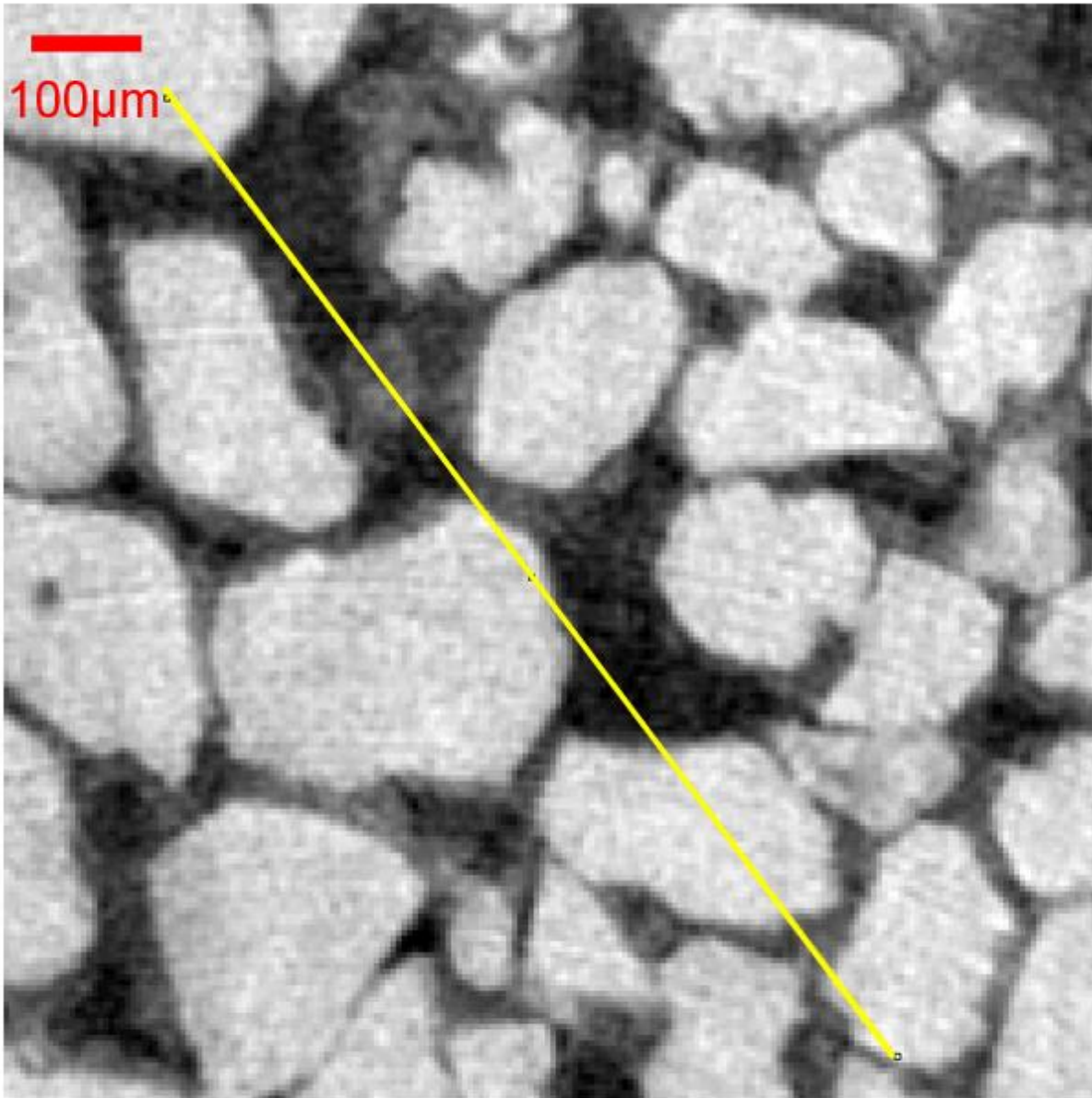
565 Figure 7. Experimental setup No. 1: (a) Schematic view; (b) picture.



566

567 Figure 8. Example of image of an unsuccessful scan due to the cell vibration,
568 obtained with the experimental setup No. 1. Voxel size: 5 μ m.

569



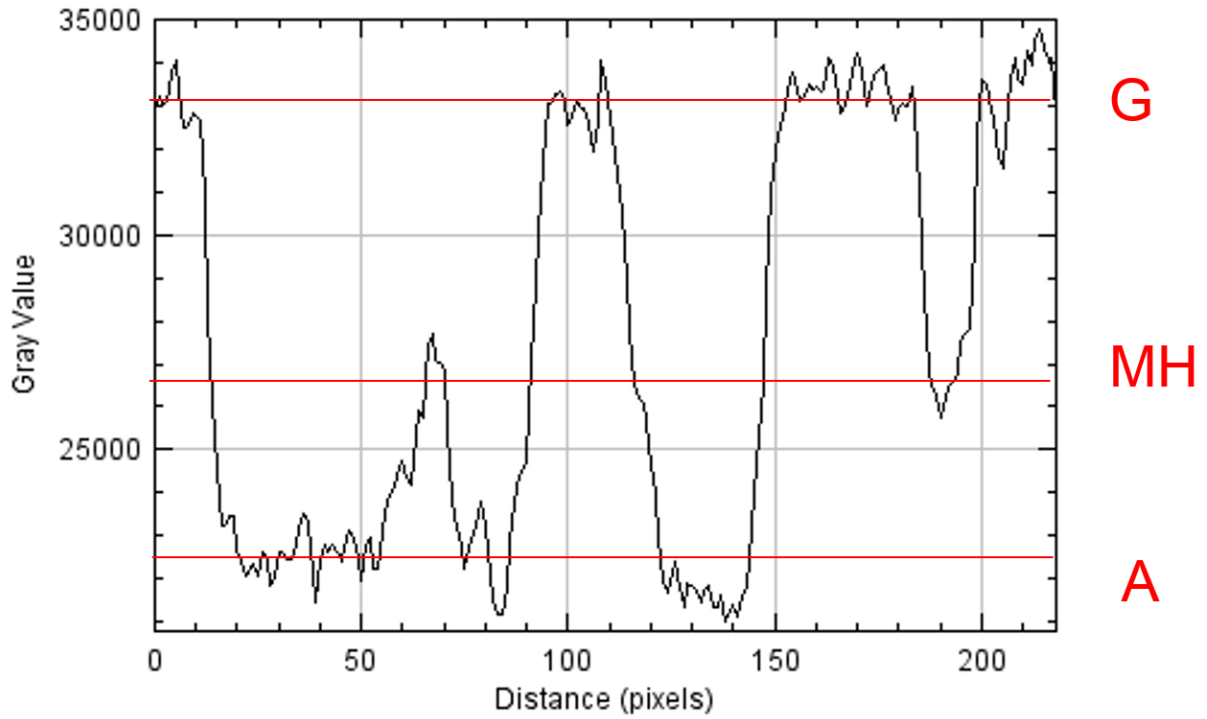
570

571 Figure 9. Example of image of MHBS obtained with the setup No. 1. Voxel size: 5 μ m.

572

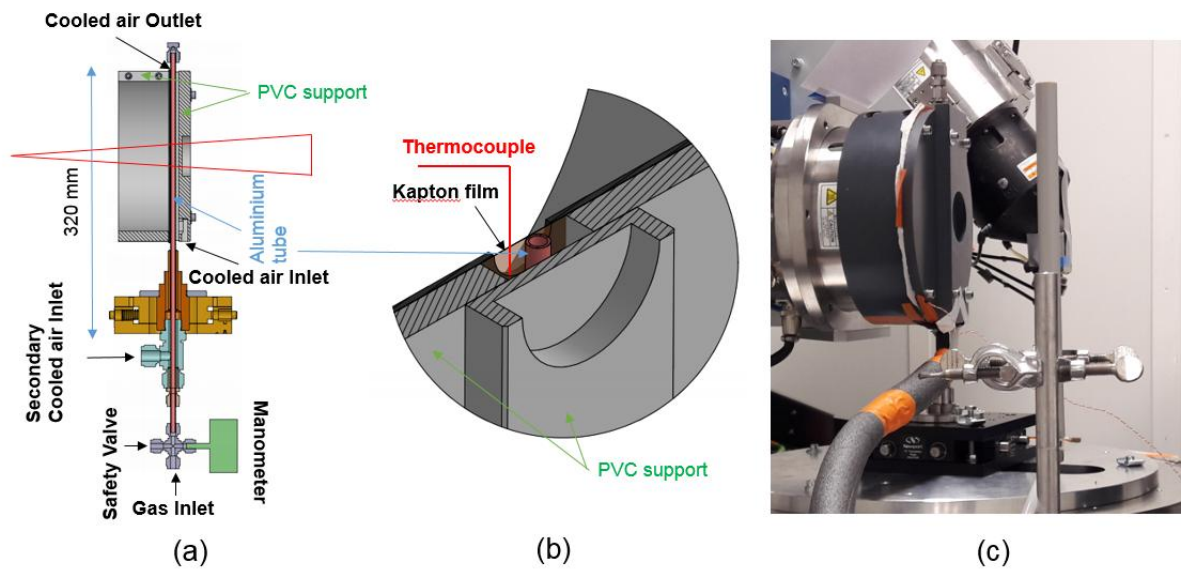
573

574



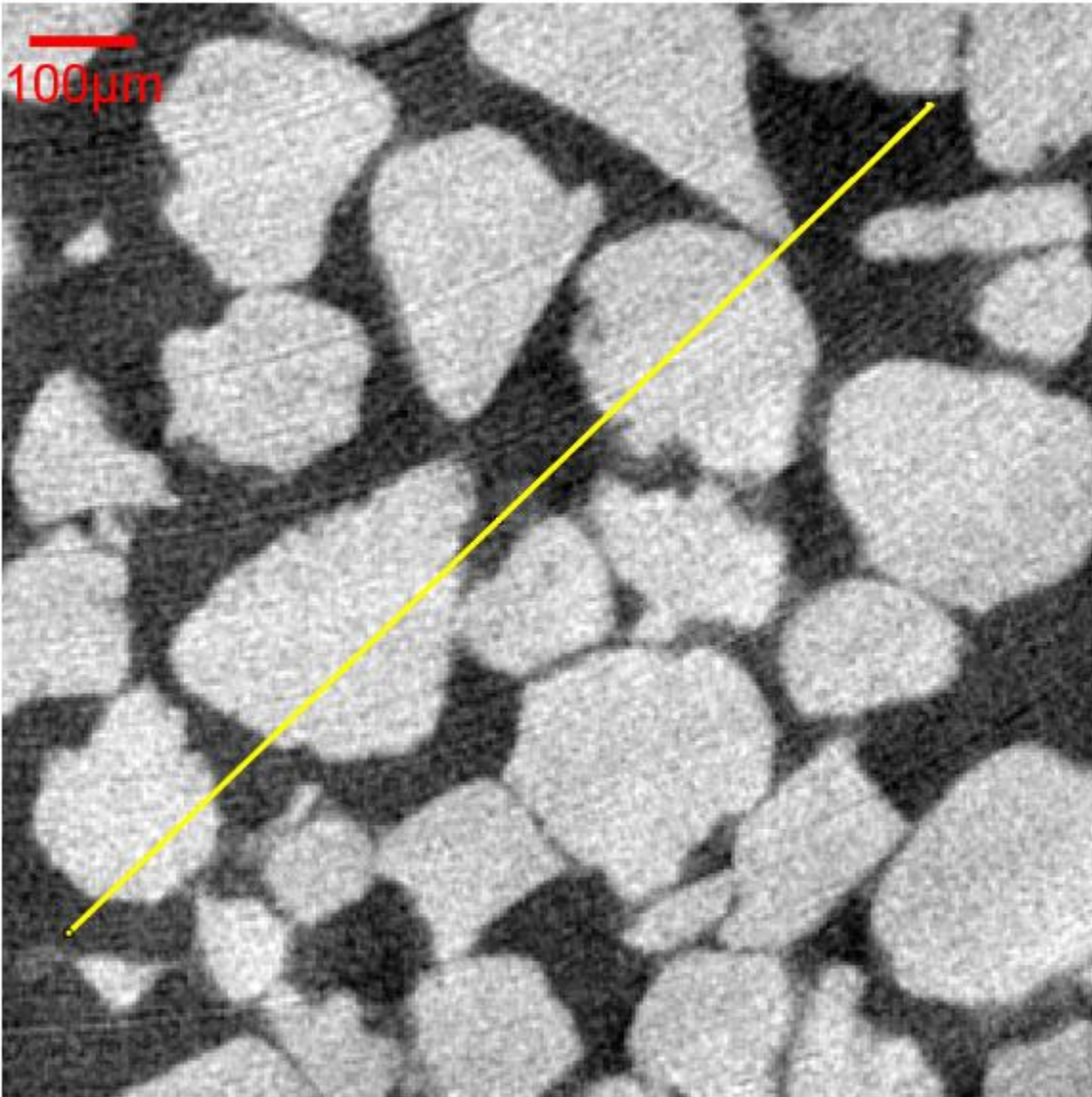
575

576 Figure 10. Gray level profile along yellow line in Figure 9.



577

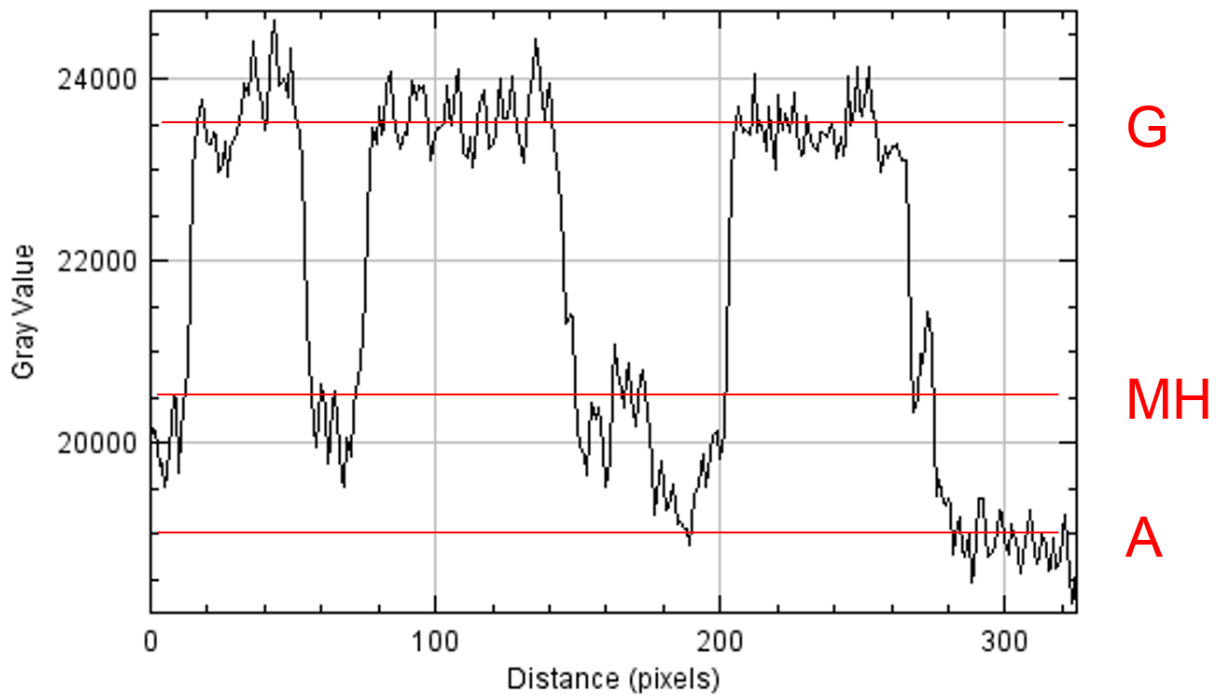
578 Figure 11. Experimental setup No. 2: (a), (b) Schematic view; (c) picture.



579

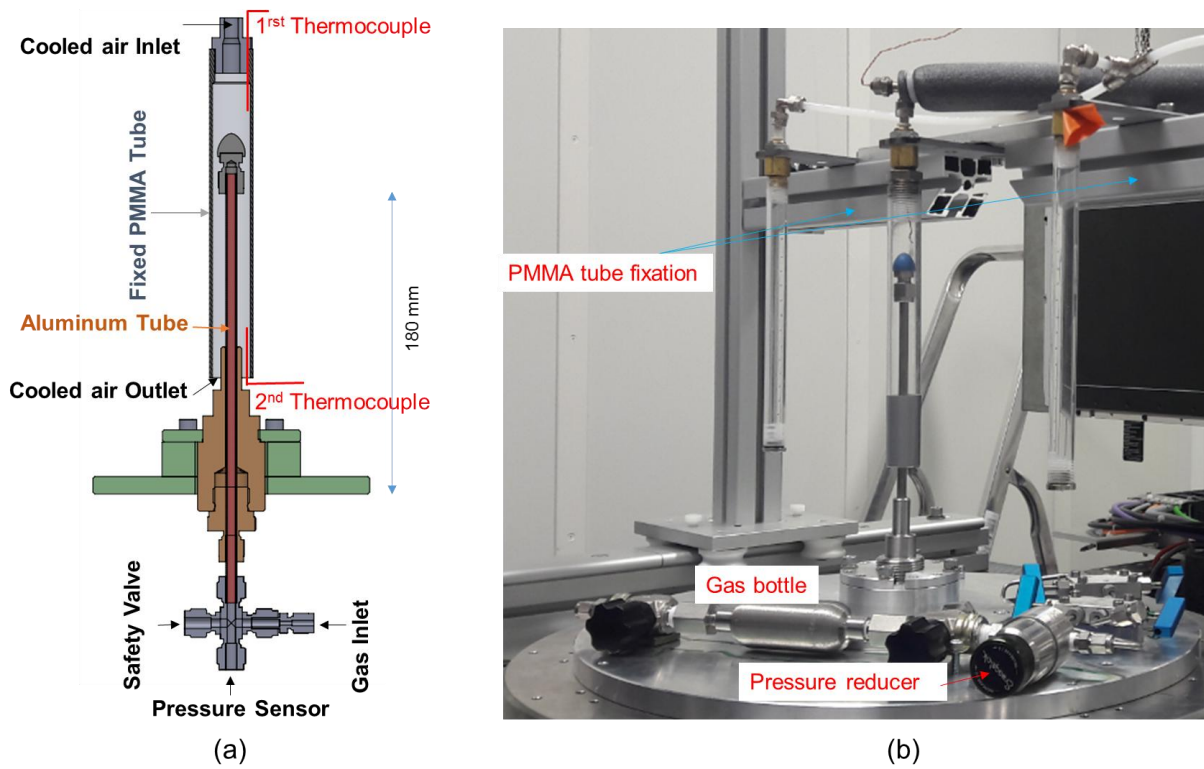
580 Figure 12. Example of image of MHBS obtained with the setup No. 2. Voxel size: 3,5

581 µm.



582

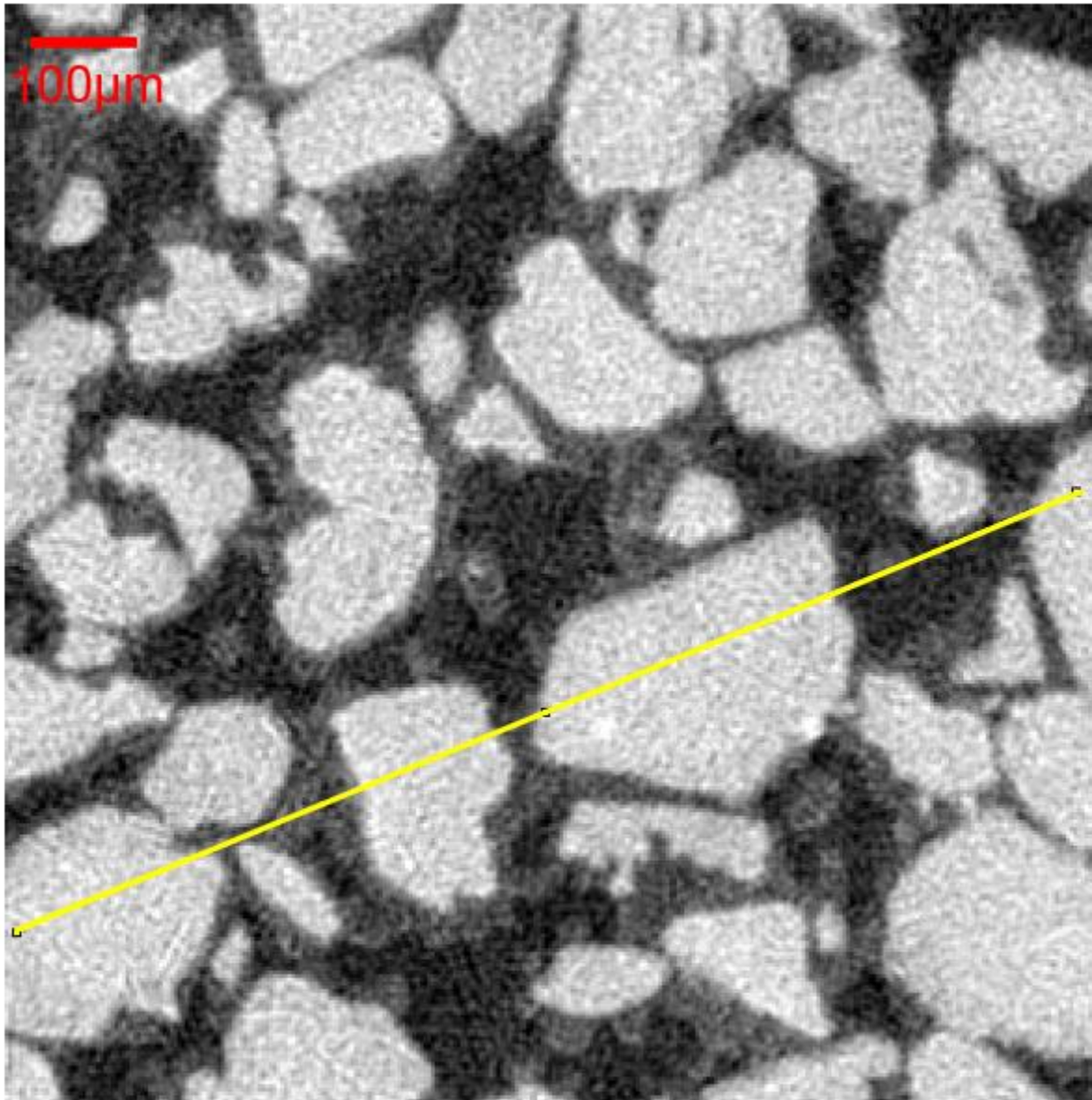
583 Figure 13. Gray level profile along yellow line in Figure 12.



584

585 Figure 14. Experimental setup No. 3: (a) Schematic view; (b) picture.

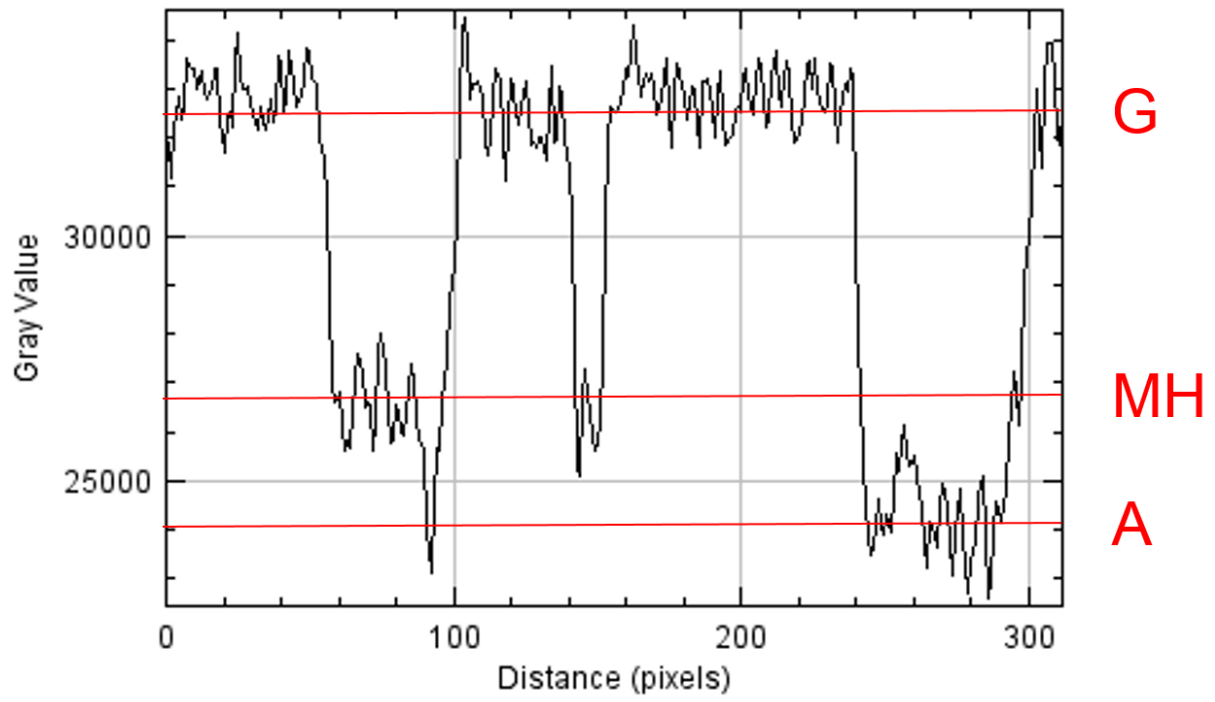
586



588

589 Figure 15. Example of XRCT image of MHBS obtained with the setup No. 3. Voxel
590 size: 4 μm.

591

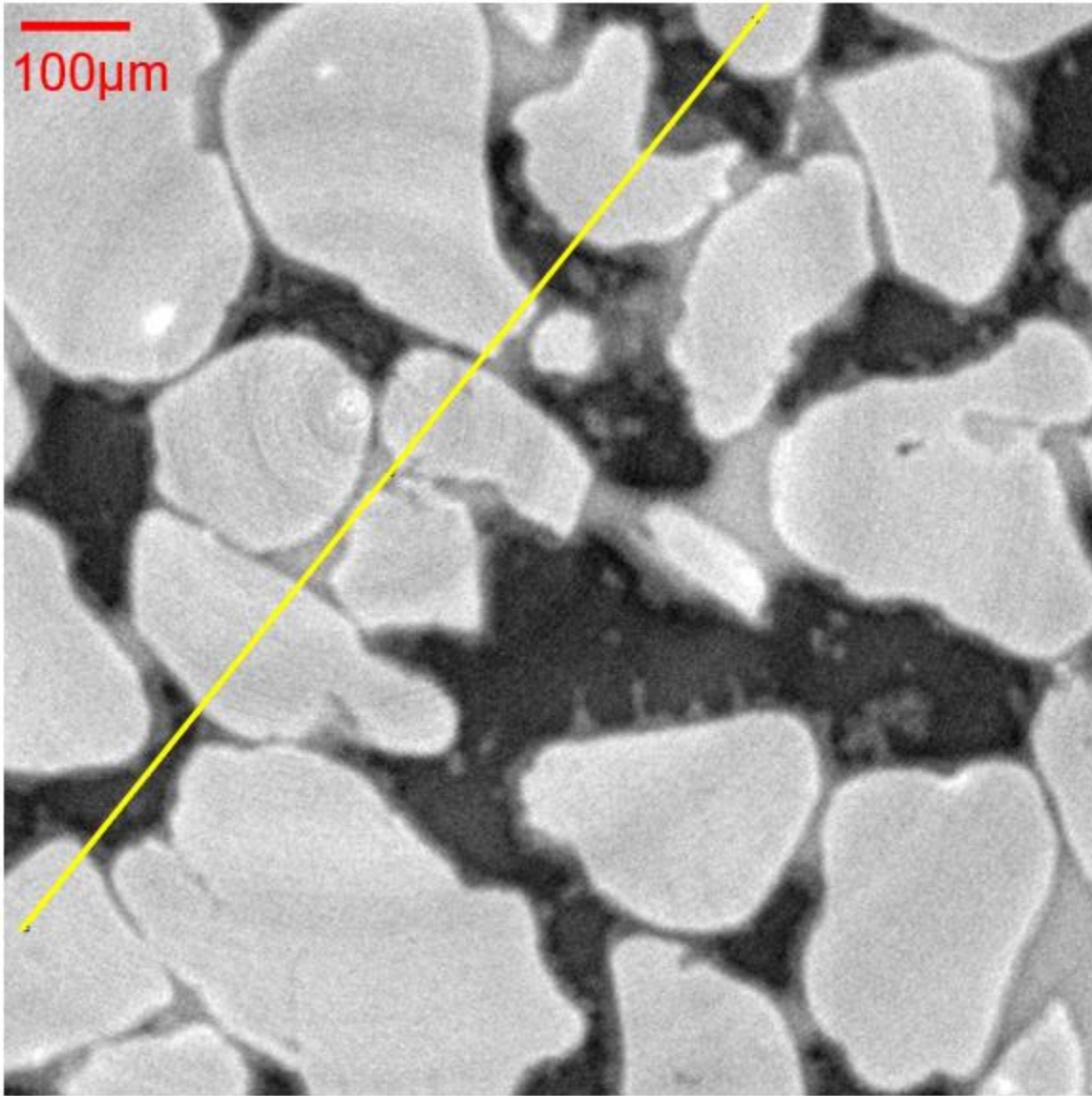


592

593 Figure 16. Gray level profile along yellow line in Figure 15.

594

595

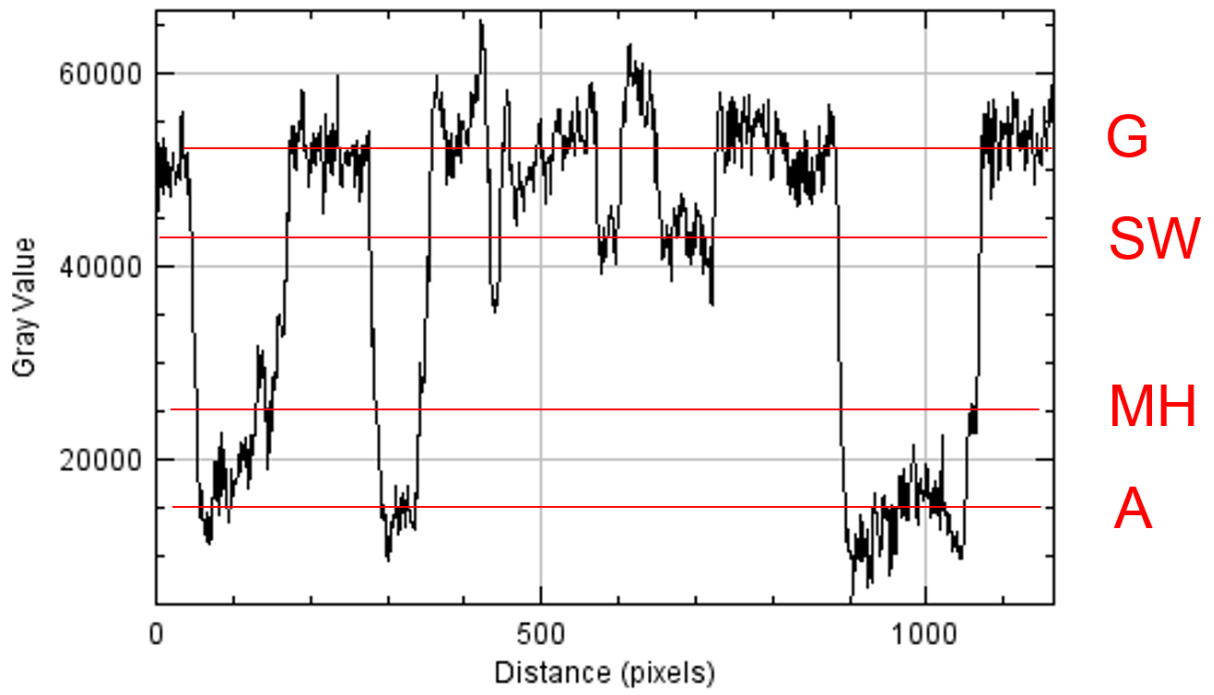


596

597 Figure 17. Example of SXRCT image of MHBS obtained with the setup No. 3. Voxel

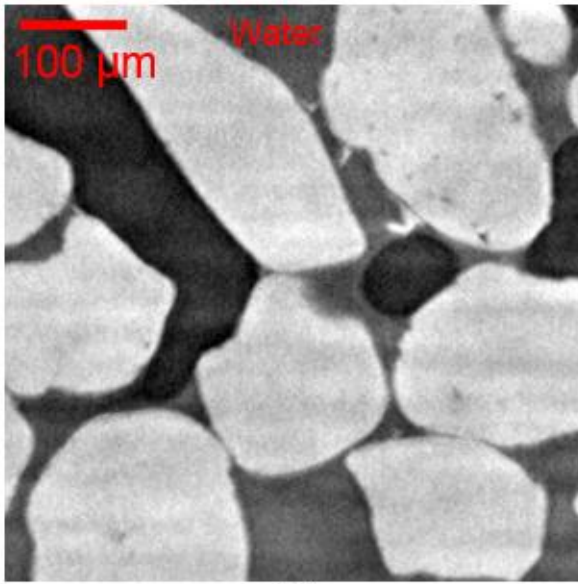
598 size: 0.9 µm.

599

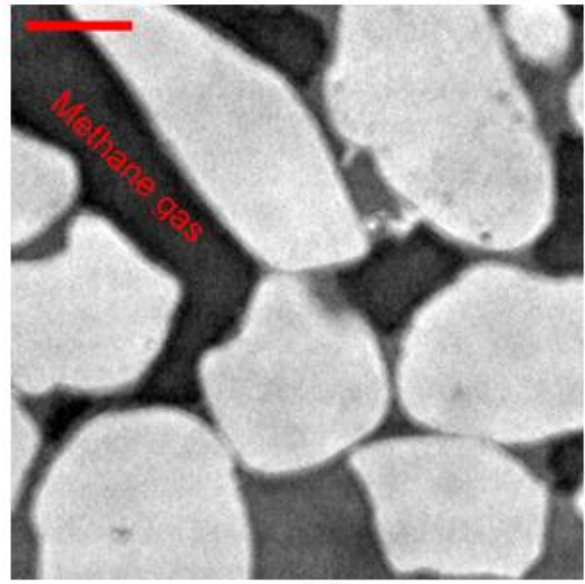


600

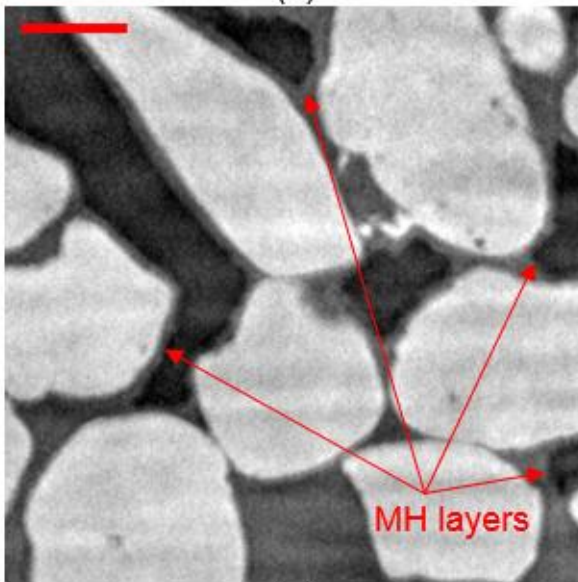
601 Figure 18. Gray level profile along yellow line in Figure 17.



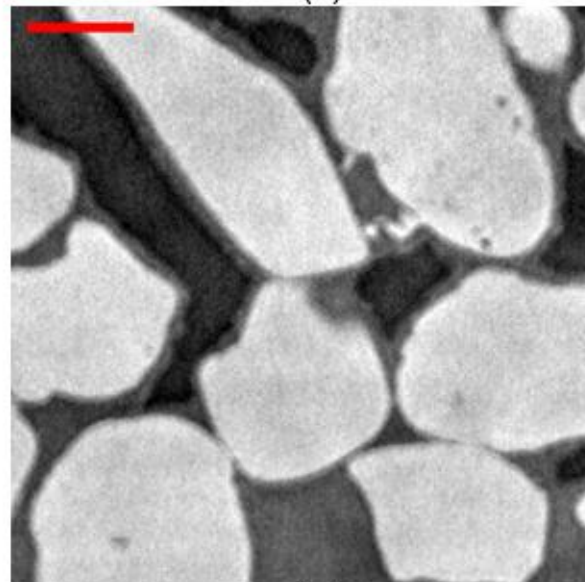
(a)



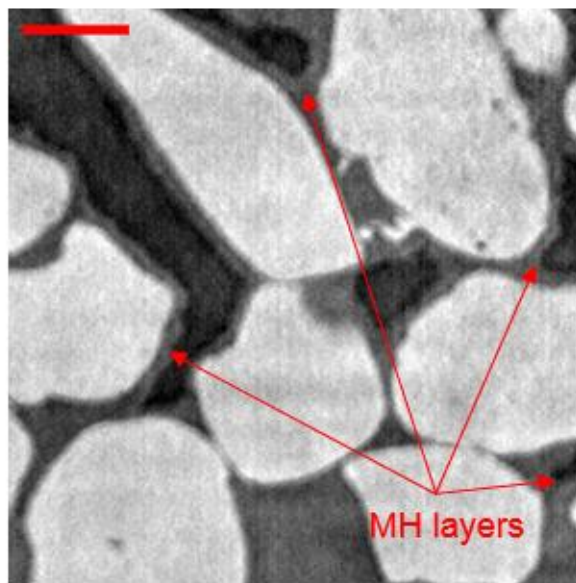
(b)



(c)



(d)



(e)

603 Figure 19. Vertical cross-section showing the MH formation (tap water) at: (a) $t = 0.3$
604 h; (b) $t = 0.8$ h; (c) $t = 2.2$ h; (d) $t = 4.3$ h; (e) $t = 6.0$ h.

605

606 **References**

- 607 Alavoine, A., Dangla, P., Pereira, and J.M. 2020. “Fast Fourier transform-based
608 homogenisation of gas hydrate bearing sediments”. *Géotechnique Letters*, 10, 367-
609 376.
- 610 Boswell, R., Moridis, G., Reagan, M., Berkeley, L., and Collett, T. S. 2011. “Gas
611 hydrate accumulation types and their application to numerical simulation”. In
612 *Proceedings of the 7th International Conference on Gas Hydrates* (p. 12).
- 613 Chand, S., Minshull, T. A., Gei, D., and Carcione, J. M. 2004. “Elastic velocity models
614 for gas-hydrate-bearing sediments - A comparison”. *Geophysical Journal
615 International*, 159(2), 573–590. <https://doi.org/10.1111/j.1365-246X.2004.02387.x>
- 616 Chaouachi, M., Falenty, A., Sell, K., Enzmann, F., Kersten, M., Haberth, D., and
617 Werner, F. K. 2015. “Microstructural evolution of gas hydrates in sedimentary
618 matrices observed with synchrotron X-ray computed tomographic microscopy”.
619 *Geochemistry, Geophysics, Geosystems*, 16, 1711–1722. <https://doi.org/10.1002/2015GC005811>
- 621 Chen, X., and Espinoza, D. N. 2018. “Ostwald ripening changes the pore habit and
622 spatial variability of clathrate hydrate”. *Fuel*, 214, 614–622.
623 <https://doi.org/10.1016/j.fuel.2017.11.065>
- 624 Clayton, C. R. I., Priest, J. A., and Best, A. I. 2005. “The effects of disseminated
625 methane hydrate on the dynamic stiffness and damping of a sand”. *Géotechnique*,
626 55(6), 423–434. <https://doi.org/10.1680/geot.2005.55.6.423>
- 627 Collett, T. S., Johnson, A. H., Knapp, C. C., and Boswell, R. 2009. “Natural gas
628 hydrates: A review”. *The American Association of Petroleum Geologists*, 89, 146–
629 219. <https://doi.org/10.1306/13201101M891602>
- 630 Dai, S., Santamarina, J. C., Waite, W. F., and Kneafsey, T. J. 2012. “Hydrate
631 morphology: Physical properties of sands with patchy hydrate saturation”. *Journal of
632 Geophysical Research B: Solid Earth*, 117(11).
633 <https://doi.org/10.1029/2012JB009667>
- 634 Dvorkin, J., and Lavoie, D. 1999. Elasticity of marine sediments: “Rock physics
635 modeling”. *Geophysical Research Letters*, 26(12), 1781–1784.
636 <https://doi.org/http://dx.doi.org/10.1029/1999GL900332>
- 637 Dvorkin, J., and Nur, A. 1996. “Elasticity of high-porosity sandstones: Theory for two
638 North Sea data sets”. *Geophysics*, 61(5), 890–893.
639 <https://doi.org/10.1190/1.1444059>
- 640 Dvorkin, J., Helgerud, M. B., Waite, W. F., Kirby, S. H., and Nur, A. 2000.
641 “Introduction to Physical Properties and Elasticity Models: Chapter 20”.
642 https://doi.org/10.1007/978-94-011-4387-5_20

643 Helgerud, M. B., Dvorkin, J., and Nur, A. 1999. "Elastic-wave velocity in marine
644 sediments with gas hydrates: Effective medium modeling". *Geophysical Research*
645 *Letters*, 26(13), 2021–2024. <https://doi.org/http://dx.doi.org/10.1029/1999GL900421>

646 Kerkar, P., Jones, K. W., Kleinberg, R., Lindquist, W. B., Tomov, S., Feng, H., and
647 Mahajan, D. 2009. "Direct observations of three dimensional growth of hydrates
648 hosted in porous media". *Applied Physics Letters*, 95(2), 2007–2010.
649 <https://doi.org/10.1063/1.3120544>

650 Kerkar, P. B., Horvat, K., Jones, K. W., and Mahajan, D. 2014. "Imaging methane
651 hydrates growth dynamics in porous media using synchrotron X-ray computed
652 tomography". *Geochemistry Geophysics Geosystems*, 15, 4759–4768.
653 <https://doi.org/10.1002/2014GC005373>

654 King, A., Guignot, N., Zerbino, P., Boulard, E., Desjardins, K., Bordessoule, M.,
655 Leclercq, N., Le, S., Renaud, G., Cerato, M., Bornert, M., Lenoir, N., Delzon, S.,
656 Perrillat, J.-P., Legodec, Y., and Itié, J.-P. 2016 "Tomography and imaging at the
657 PSICHE beam line of the SOLEIL synchrotron," *Review of Scientific Instruments*,
658 87(9).

659 Le, T. X., Aïmediu, P., Bornert, M., Chabot, B., Rodts, S., and Tang, A. M. 2019.
660 "Effect of temperature cycle on mechanical properties of methane hydrate-bearing
661 sediment". *Soils and Foundations*, 59(4), 814-827.
662 <https://doi.org/10.1016/j.sandf.2019.02.008>

663 Le, T. X., Rodts, S., Hautemayou, D., Aïmediu, P., Bornert, M., Chabot, B., and
664 Tang, A. M. 2020. "Kinetics of methane hydrate formation and dissociation in sand
665 sediment". *Geomechanics for Energy and the Environment*, 100103.
666 <https://doi.org/10.1016/j.gete.2018.09.007>

667 Le, T.X. 2019. "Experimental study on the mechanical properties and the
668 microstructure of methane-hydrate bearing sandy sediments". PhD Thesis of
669 Université Paris-Est.

670 Lei, L., Seol, Y., and Jarvis, K. 2018. "Pore-Scale Visualization of Methane Hydrate-
671 Bearing Sediments With Micro-CT". *Geophysical Research Letters*, 45(11), 5417–
672 5426. <https://doi.org/10.1029/2018GL078507>

673 Lei, L., Seol, Y., Choi, J. H., and Kneafsey, T. J. 2019. "Pore habit of methane
674 hydrate and its evolution in sediment matrix–Laboratory visualization with phase-
675 contrast micro-CT". *Marine and Petroleum Geology*, 104, 451-467.

676 Nguyen-Sy, T., Tang, A.M., To, Q.D., and Vu, M.N. 2019. "A model to predict the
677 elastic properties of gas hydrate-bearing sediments". *Journal of Applied Geophysics*,
678 169, 154 – 164. <https://doi.org/10.1016/j.jappgeo.2019.05.003>.

679 NIST XCOM: <https://physics.nist.gov/PhysRefData/Xcom/html/xcom1.html>

680 Paganin, D., Mayo, S. C., Gureyev, T. E., Miller, P. R., and Wilkins, S. W. 2002.
681 "Simultaneous phase and amplitude extraction from a single defocused image of a
682 homogeneous object". *Journal of microscopy*, 206(1), 33-40.

683 Priest, J. A., Rees, E. V. L., and Clayton, C. R. I. 2009. "Influence of gas hydrate
684 morphology on the seismic velocities of sands". *Journal of Geophysical Research:*
685 *Solid Earth*, 114(11). <https://doi.org/10.1029/2009JB006284>

686 Sloan, E. D. and Koh, C.A. 2008. "Clathrate Hydrates of Natural Gases".

687 Swinehart, D. F. 1962. "The Beer-Lambert Law". *Journal of Chemical Education*,
688 39(7), 333. <https://doi.org/10.1021/ed039p333>

689 Ta, X. H., Yun, T. S., Muhunthan, B., and Kwon, T. 2015. "Observations of pore-scale
690 growth patterns of carbon dioxide hydrate using X-ray computed microtomography".
691 *Geochemistry Geophysics Geosystems*, 912–924.
692 <https://doi.org/10.1002/2014GC005675>

693 Taleb, F., Garziglia, S., and Sultan, N., 2018. "Hydromechanical Properties of Gas
694 Hydrate-Bearing Fine Sediments From In Situ Testing". *Journal of Geophysical*
695 *Research: Solid Earth*, 123(11), 9615-9634.

696 Taleb, F., Lemaire, M., Garziglia, S., Marsset, T., and Sultan, N., 2020. "Seafloor
697 depressions on the Nigerian margin: Seabed morphology and sub-seabed hydrate
698 distribution". *Marine and Petroleum Geology* 114, 104175.

699 Waite, W., Winters, W. J., and Mason, D. H. 2004. "Methane hydrate formation in
700 partially water-saturated Ottawa sand". *American Mineralogist*, 89, 1202–1207.

701 Yang, L., Zhao, J., Liu, W., Li, Y., Yang, M., and Song, Y. 2015. "Microstructure
702 Observations of Natural Gas Hydrate Occurrence in Porous Media Using Microfocus
703 X-ray Computed Tomography". *Energy & Fuels*, 29(8), 4835–4841.
704 <https://doi.org/10.1021/acs.energyfuels.5b00881>

705 Zhao, J., Yang, L., Liu, Y., and Song, Y. 2015. "Microstructural characteristics of
706 natural gas hydrates hosted in various sand sediments". *Royal Society of Chemistry*,
707 17(35), 22632–22641. <https://doi.org/10.1039/c5cp03698d>

708